Experimental study of the nonlinear flow characteristics of fluid in 3D rough-walled fractures during shear process

Changsheng Wang[1, 2], Yujing Jiang[1, 2, *], Richeng Liu, [2, 3] Chen Wang[2], Zhenyu Zhang[4], Satoshi Sugimoto[2]

[1] *State Key Laboratory of Mining Disaster Prevention and Control Co-founded by Shandong Province and the Ministry of Science and Technology, Shandong University of Science and Technology, China*

[2] *School of Engineering, Nagasaki University, Nagasaki 852-8521, Japan*

[3] *State Key Laboratory for Geomechanics and Deep Underground Engineering, China University of Mining and Technology, Xuzhou 221116, P.R. China*

[4] *State Key laboratory of Coal Mine Disaster Dynamics and Control, Chongqing University, Chongqing 400044, P.R. China*

Corresponding author: Yujing Jiang

E-mail address: jiang@nagasaki-u.ac.jp (Y. Jiang).

Keywords: Rough-walled fractures; shear-flow test; nonlinear flow; critical hydraulic gradient; normalized transmissivity; visualization.

List of symbols

A	Cross-sectional area of a fracture
a	Linear coefficient in the Forchheimer's Law
b	Nonlinear coefficient in the Forchheimer's Law
b_{h}	Hydraulic aperture
d	Shear displacement
d_{contra}	Minimum normal displacement
d_{dilation}	Dilation of the fracture
d_{normal}	Ultimate normal displacement

d_{peak} Peak shear displacement
E Nonlinear effect factor
J Hydraulic gradient
J_c Critical hydraulic gradient
JRC Joint roughness coefficient
k Fracture permeability
K_s Shear stiffness
L Fracture length
P Hydraulic pressure
Q Volumetric flow rate
Re Reynolds number
Re_c Critical Reynolds number
T Transmissivity
T/T_0 Normalized transmissivity
w Width of a fracture
z_i Coordinates of the fracture surface profile
Z_2 Dimensionless roughness parameter
ρ Fluid density
μ Dynamic viscosity
σ_n Normal stress
τ_{peak} Peak shear strength

Abstract: To understand the influence of shear on the hydraulic properties of rock fractures, shear-flow tests were carried out on rock fractures with different surface roughnesses. Each rough-walled fracture was replicated in four specimens, which were sheared at different displacements under normal stresses that varied from 0.5 MPa to 2.0 MPa. At each shear displacement, a series of hydraulic tests with different hydraulic gradients were performed, and the nonlinear flow regimes of the fluid within the fractures were investigated. The results show that Forchheimer's law can well describe the nonlinear relationship between the flow rate and the hydraulic gradient in rough-walled fractures. Both the linear coefficient and nonlinear coefficient decrease during shearing but increase as the normal stress increases. The critical hydraulic gradient increases with an increase in the shear displacement and normal stress. With an increase in the joint roughness coefficient, the critical hydraulic gradient decreases. The normalized transmissivity exhibits a strong correlation with the Reynolds number. As the shear displacement increases, the fitted curves of the normalized transmissivity versus the Reynolds number shift upward but the curves shift downward with an increase in normal stress. Additionally, the Forchheimer coefficient decreases with an increase in the shear displacement but increases with an increase in the applied normal stress. Visualization tests show that the number of flow paths is large when the shear displacement is small due to various distributions of the contact areas and that the flow of dyed water over the entire fracture decreases. As the shear displacement increases, the flow resistance decreases due to the shear dilation-induced increase in the aperture, and the advantage channel flow is distinct in the fracture. The contact ratio rapidly decreases as the shear displacement increases from 1 to 3 mm and then slightly varies with a continuously increasing maximum shear displacement of 9 mm.

1. Introduction

Knowledge of fluid flow in fractured rock masses is critical to natural gas production, geological sequestration of carbon dioxide, radioactive waste disposal and geothermal energy extraction (Wu et al. 2011; Babadagli et al. 2015; Leung and Zimmerman, 2012; Zhou et al. 2015; Wang et al. 2017; Chen et al. 2017). Rock masses are a typical dual-porosity system that includes a rock matrix surrounded by fracture networks. Fracture networks are considered the main channels for fluid flow due to their substantially higher permeability compared with a rock matrix (Liu et al. 2011; Wang et al. 2016; Wei and Xia 2017). Thus, understanding the fluid flow properties of rock fractures is fundamental to the performance and safety assessment of these types of engineering projects.

Individual fractures in natural rock masses form fracture networks; therefore, understanding fluid flow in a single fracture is a foundation for modeling flow via complex fracture networks (Rong et al. 2016). Generally, fluid flow in a single fracture obeys the well-known Navier–Stokes (NS) equations (Zimmerman and Bodvarsson, 1996; Koyama et al. 2008). However, due to complex nonlinear partial differential equations and irregular fracture morphology, solving the NS equations is difficult (Brush and Thomson, 2003; Javadi et al.2010; Huang et al. 2017). To circumvent this problem, for steady laminar flow through single fractures, the inertial terms of the NS equations can be considered negligible, and the NS equations can be simplified to the cubic law (Zhang and Nemcik 2013; Tzelepis et al. 2015; Li et al. 2016), whicn can be written as:

$$Q = -\frac{\Delta P}{L\mu}\,\frac{w{b_h}^3}{12} \tag{1}$$

where Q is the volumetric flow rate, ΔP is the pressure drop in the flow direction, w is the fracture width, b_h is the hydraulic aperture, L is the fracture length over which the pressure drop occurs, and μ is the viscosity of the fluid. The fracture transmissivity T is equal to the term $w{b_h}^3/12$ in Eq. (1), which can be written as (Brown et al. 1995; Olsson and Barton 2001):

$$T = k\mathrm{A} = \frac{w{b_h}^3}{12} \tag{2}$$

where $k = {b_h}^2/12$ and $\mathrm{A} = wb_h$, where k is the permeability of the fracture and A is the cross-sectional area. The cubic law shows a linear relationship between the flow rate and the pressure drop and assumes that the fracture surface can be approximated by the flat parallel plate model. However, the cubic law is derived from disregarding the inertia effects, which is valid for laminar flow with a sufficiently low flow rate. In nature, the rock fracture in realistic situations exhibits a complexity of the geometrical characteristics on their surfaces, which causes deviations from the cubic law. In this case, use of the cubic law to calculate fluid flow overestimates the transmissivity of rock fractures (Zimmerman and Bodvarsson 1996; Oron and Berkowitz 1998; Wang et al. 2015; Zhang et al. 2017; Yu et al. 2017). Therefore, many studies adopted Forhheimer equations to describe the nonlinear flow through rough−walled rock fractures (Forchheimer 1901):

$$J = aQ + bQ^2 \tag{3}$$

$$a = -\mu/\rho g k \mathrm{A},\ b = -\beta\mu/\rho g \mathrm{A}^2 \tag{4}$$

where J = $\Delta P/\rho g\mathrm{L}$, J is the hydraulic gradient, ρ is the fluid density, g is the gravitational acceleration and β is the Forchheimer coefficient. a and b are coefficients that represent the pressure drops caused by linear effects and nonlinear effects, respectively. Eq. (3) can well describe the nonlinear flow behaviors in fractures, which has been verified to be valid via experiments, numerical simulations, and theoretical analyses (Moutsopoulos 2009; Qian et al. 2011; Cherubini et al. 2012; Adler et al. 2013). However, the mechanisms that trigger nonlinearity in rough-walled rock fractures are not completely understood because this equation cannot consider the effects of the fracture surface roughness and contact area on the flow behavior (Rong et al. 2017). Chen et al. (2000) reported that the fracture surface roughness, contact area and tortuosity may cause nonnegligible inertial forces that cause deviation from the cubic law. Similar conclusions were obtained by Brush and Thomson (2003) and Li et al.

(2008), who concluded that complicated flow patterns cause inertial losses even with laminar flow.

Previous studies have investigated many factors that can influence the nonlinear flow characteristics in fractures, such as normal stress (Rabjith and Darlington 2007; Zhang and Nemcik 2013; Zhou et al. 2015; Chen et al. 2015), fracture surface roughness (Javadi et al. 2010; Wang et al.2016; Liu et al. 2016), fracture aperture (Koyama et al .2006; Liu et al. 2016a) and fracture intersection (Kosakowski and Berkowitz 1999; Liu et al. 2016a; Liu et al. 2016c, Yin et al. 2018).The critical Reynolds number (Re_c) and critical hydraulic gradient (J_c) were commonly defined in these studies to quantify the onset of nonlinear fluid flow. Rabijth and Darlington (2007) observed that Re_c decreases from 31.29 to 28.77 with an inceaese in the confining stress from 1.0 MPa to 5.0 MPa. Wang et al. (2016) discovered that Re_c decreases following an exponential function as the fracture surface roughness increases. Liu et al. (2016b) investigated the effect of the fracture aperture on the nonlinear flow regimes. The results show that J_c decreases by approximately four orders of magnitude with an increase in the fracture aperture from 1.0 mm to 10.0 mm. Kosakowski and Berkowitz (1999) established numerical models with different single fracture intersection geometries to study the validity of Darcy’s law. The results indicate that the nonlinear inertial effects become important at Reynolds numbers (Re) from 1 to 100. Liu et al. (2016a) estimated the influence of the number of fracture intersections on the nonlinear flow in fracture networks. The results show that J_c initially significantly decreases and then slowly decreases with a power law function with an increase in the number of fracture intersections from 1 to 12.

However, most previous studies are focused on flow characterizations of well-mated fractures. Note that the fractures are commonly subjected to shear, which is caused by various natural and human activities, such as earthquakes, underground excavations and geothermal energy reservoir productions. Shear displacement can cause a change in the contact area and the aperture distribution, which is an important issue that affects flow and transport behavior in rough-walled fractures. (Yeo et al. 1998; Esaki et al. 1999; Yin et al. 2017). Therefore, investigating the effects of the shear process on the nonlinear flow characteristics of fractures is important. Javadi et al. (2014) conducted coupled shear-flow tests on three granite specimens to investigate the variation in Re_c during the shear process under different normal stresses. The results showed that Re_c ranges from 0.001 to 25 as the shear displacement increases from 0 to 20 mm. However, the effect of the joint roughness coefficient on nonlinear flow regimes in fractures during shear was negligible. Similar shear-flow tests were also conducted by Rong et al. (2016), who performed shear-flow tests on six granite fractures with the joint roughness coefficient (JRC) = 6.67 ~ 8.18 under different normal stresses to study the nonlinear fluid flow characteristics during shear. They suggested that Re_c ranges from 1.5 to 13.0 as the shear displacement increases from 0 to 10.9 mm. However, the range of JRC (8.18 – 6.67 = 1.51) was very small, and the effect of the JRC on the nonlinear fluid flow behavior was not clearly presented. Recently, Yin et al. (2017) experimentally analyzed the influences of the shear displacement and normal stress on the nonlinear flow behavior of fluid through 3D rough-walled rock fractures with JRC = 15.17 and discovered that J_c increased with an increase in the shear displacement and decreased with an increase in the normal stress. As previously described, most previous studies have focused on the effect of the normal stress on the nonlinear fluid flow characteristics during shear. However, few studies have focused on the influence of the fracture surface roughness on the characteristics of nonlinear fluid flow through fractures during shear.

This study systematically investigates the effects of the fracture surface roughness, normal stress and shear displacement on the nonlinear flow characteristics of a single fracture. Four types of granite fractures with different surface characteristics were employed in the tests. At each shear step, high precision hydraulic tests were conducted with different hydraulic gradients. The nonlinear flow regimes are analyzed in terms of the fracture surface roughness and normal stress of fractures during shear. Additionally, to estimate the influence of the shear process on the nonlinear flow characteristics in rough-walled fractures, a visualization test was conducted on fracture G3-1 to determine how the channeling flow and contact area affect the nonlinear flow regimes.

2. Experimental method

2.1 Specimen preparation and roughness measurement

In this study, four granite specimens were collected from the Omarugawa power station in Miyazaki prefecture, Japan. The four specimens were cut and polished to cuboid specimens with the following dimensions: length of 200 mm, width of 100 mm and height of 100 mm. An artificial tensile fracture was created using the Brazilian test. During the test, a normal stress of 10 kN was applied to the specimen, and lateral stress was then applied using V-shaped wedges to a constant horizontal stress of 120 kN. The split was extended until a tensile fracture formed. Four fractures (labeled G1, G2, G3 and G4) with different surface geometries are shown in Fig. 1. One half of each specimen was chosen as the model to cast another half using resin material. The upper and lower halves of the specimens were then manufactured based on the resin replica. For visual shear-flow tests, a transparent acrylic specimen was prepared as the upper half, and the plaster specimen was fixed as the lower half. Each rough-walled fracture was replicated in four specimens. The artificial fracture specimens were manufactured using mixtures of plaster, water and retardant with a weight ratio of 1: 0.2: 0.005. The physico-mechanical properties of these rock-like specimens are shown in Table 1.

The four fracture surfaces of the specimens were scanned at resolutions of $\pm 20\ \mu m$ and $\pm 10\ \mu m$ in the x-y plane and on the z axis, respectively. Based on the scanned data, digitized fracture surfaces of the four specimens were created (Fig. 1). To quantify the surface roughness of the fracture, ten profiles parallel to the flow direction were extracted from each fracture by dividing the fracture into nine equal areas. The JRC was calculated according to the equations proposed by Tse and Cruden (1979) and written as

$$Z_2 = \left[\frac{1}{(n-1)(\Delta x)^2}\sum_{i=1}^{n-1}(z_{i+1} - z_i)^2\right]^{1/2} \tag{5}$$

$$JRC = 32.2+32.47\log Z_2 \tag{6}$$

where Z_2 is the root mean square slope of the profiles based on the extracted data, z_i represents the coordinates of the fracture surface profile, n is the number of data points, and Δx is the interval between the data points. The mean JRC values of fractures G1, G2, G3 and G4 were 3.21, 5.62, 7.36 and 12.16, respectively. The variation in frequency versus asperity height of four fracture surfaces are depicted in Fig. 2; the results show that the rougher fracture trends to generate a wider range of the asperities distribution.

2.2 Experimental apparatus

In this study, shear-flow tests were carried out using a laboratory visualization system of the shear-flow test apparatus, as shown in Fig. 3. The system mainly consists of a hydraulic-servo actuator unit, a hydraulic testing unit and a visualization unit. The hydraulic-servo actuator unit consists of two load jacks that apply the normal and shear loads via a servo-controlled hydraulic pump. The maximum applied load is 200 kN in the shear and normal direction with a precision of 99%. The hydraulic testing unit contains a water supply system, a fracture sealing system and a measurement system. Constant water pressure was applied to one side of the fracture using an air pump. A pressure transducer with a precision of 0.01 kPa was attached to the water inlet to measure the inlet water pressure. The water outlet was connected to a tube with a diameter of 10 mm and a smooth inner wall. The outlet pressure was assumed to be zero due to the relatively small flow rate. The lateral sides of the fracture were sealed using soft and elastic gel sheets, which were flexible and strong with a good sealing effect. The water that flows out of the fracture was measured using an electrical balance with a precision of 0.01 g. The most important characteristic of this apparatus is that an observation window is created above the upper part of the shear box and a normal load is applied to the specimen from the bottom of the shear-box. Hence, a coupled charged device (CCD) camera placed on top of the specimen can directly view the dyed water that flows through the transparent acrylic specimen. Many coupled shear-flow tests have been carried out using this apparatus, which shows a good sealing effect (i.e., Li et al. 2008; Koyama et al. 2008; Xiong et al. 2011).

2.3 Experimental procedures

A specimen was set in the shear box, and the shear box was fixed on the steel plate connected to the normal load jack. The lower shear box can only move in the vertical direction by the roller guide, and the upper shear box can move in the vertical and horizontal direction without rotation during shearing (Xiong et al. 2011). Two small tanks were fixed at the inlet and outlet of the specimen, which were sealed using rubber sheets on the two ends of the specimen. The lateral sides were sealed using soft and elastic gel sheets. Coupled shear-flow tests were conducted at five shear displacements d (1.0, 3.0, 5.0, 7.0 and 9.0 mm) under constant normal stresses σ_n of 0.5, 1.0, 1.5 and 2.0 MPa. The test cases and their corresponding normal stresses are shown in Table 2. The shear velocity was 0.5 mm/min. At each shear step, 7 ~ 10 constant head water flow tests were carried out. The constant water pressure was supplied using an air pump. The flow rate was measured by collecting the discharge from the outlet with a high precision electrical balance. Shear-flow tests were performed at a room temperature of approximately 20 °C. The density and dynamic viscosity of water are $\rho = 0.998 \times 10^3$ kg/m^3 and $\mu = 1.006 \times 10^{-3}$ Pa·s, respectively.

3. Experimental results and discussions

3.1 Mechanical behavior

Sixteen replicated fracture specimens with four different fracture surface roughnesses were used to conduct coupled shear-flow tests under various normal stresses. The mechanical shear behaviors and characteristics of the fractures are shown in Fig. 4, Fig. 5 and Table 2. The data clearly show that the shear stress abruptly increases to the peak at the very beginning of shear. Then, the shear stress gradually decreases to the residual stage. The peak shear displacement, d_{peak}, ranges from 0.844 mm to 1.428 mm. The peak shear strength, τ_{peak}, ranges from 0.515 MPa to 1.789 MPa for G1 (Fig. 4 (a)), from 0.652 MPa to 1.834 MPa for G2 (Fig. 4 (b)), from 0.770 MPa to 2.070 MPa for G3 (Fig. 4 (c)), and from 0.813 MPa to 2.141 MPa for G4 (Fig. 4 (d)). The peak shear strength increases with an increase in the normal stress and JRC. The influences of normal stress and JRC on shear stiffness (K_s) is plotted in Fig. 6. Shear stiffness is defined as the slope of the pre-peak stage of the shear stress-shear displacement curves. As shown in Fig. 6, K_s shows an increasing trend with an increasing normal stress and JRC.

The normal displacement is an important parameter in shear-flow tests for quantifying the permeability of fractures due to increases or decreases in the fracture aperture. As shown in Fig. 7, the normal displacement decreases at the onset of shear and then rapidly increases; however, the increasing rate decreases. The decrease in normal displacement is due to the deformation of asperities and surface interlocking. The minimum normal displacement, d_{contra}, ranges from -0.03 mm to -0.172 mm for all test cases and depends on the applied normal stress. The larger is σ_n, the larger is d_{contra}. With continuously increasing shear displacement, the normal displacement increases due to shear dilation. The dilation causes the contact area to significantly decrease due to the overriding and sliding of the contact asperities. At this stage, the aperture between the opposite surfaces rapidly increases, which causes the permeability to substantially increase (Rong et al. 2016). The dilation increasing rate decreases by abrading some rougher asperities until the residual stage is reached. The ultimate normal displacement d_{normal} (corresponds to a shear displacement of 9.0 mm), ranges from 0.560 mm to 2.467 mm as listed in Table 2. The results show that d_{normal} increases with increasing normal stress, and the rougher fracture shows a larger dilation in the same test conditions.

The shear stress an normal deformation during the shear process exhibit a three-stage behavior (Xiong et al. 2011). First, the shear stress rapidly increases to the peak value, while the normal displacement reaches the maximum negative value. Second, the shear stress gradually decreases, while the normal displacement rapidly increases. Last, the shear stress and normal displacement reach the residual values in the third stage, during which the rate of decrease of the shear stress decreases, and the normal displacement continues to increase at a lower gradient. Our test results have similar trends to those in previous studies (Li et al. 2008; Koyama et al. 2008; Xiong et al. 2011; Javadi et al. 2014; Rong et al. 2016).

3.2 Fluid flow behavior

3.2.1 Effect of normal stress

In this section, eighty individual hydraulic tests based on the sixteen specimens were conducted with d = 1, 3, 5, 7 and 9 mm. To avoid the influence of gouge materials on the fluid flow behavior during the shear process, the shear-flow tests were conducted at a small range of normal stresses (0.5 ~ 2.0 MPa). During the tests, only a small amount of gouge material was observed. Therefore, the effect of the gouge material on the fluid flow is negligible.

Fig. 7 shows the relationships between the hydraulic gradient J and the flow rate Q, which corresponds to different shear displacement for fractures G1 at different constant values of σ_n (other test data sets are attached in "Appendix A, Fig. A1"). The relationship between J and Q exhibits distinct nonlinear characteristics. The Forchheimer equation fits the data well with a residual squared (R^2) greater than 0.98 in all cases. With an increase in d, the slopes of the J - Q curves become flatter as a result of fracture dilation ($d_{dilation}$) during shear. At a given shear displacement, as σ_n increases,

Q decreases with nearly the same hydraulic gradient. For a higher σ_n, this phenomenon indicates that a larger hydraulic gradient is required to achieve the same flow rate. Note that the water flowed from a relatively large tank on the sealed side boundary into the relatively small void space of the fractures during the hydraulic tests. With a high hydraulic gradient, the fluid may flow back and influence the nonlinear flow characteristics. However, this is difficult to avoid using the current techniques. In future studies, we will attempt to decrease this system error.

Forchheimer's law is the most extensively employed mathematical description of the nonlinear flow in fractures (Zimmerman et al. 2004; Zhang and Nemcik 2013; Javadi et al. 2014; Wang et al.2016; Rong et al. 2016; Yin et al. 2017). Based on Eq. (3), the linear coefficient a and nonlinear coefficients b were calculated, as plotted in Fig. 8 and Fig. 9, respectively. Both a and b decrease with an increase in d, and the decrease extent at d from 1 to 3 mm is more significant than the reduction in the range from 3 to 9 mm. The decrease in a with d from 1 to 9 mm was approximately 0.5 ~ 1.0 orders of magnitude, and the decrease in b was approximately 2.0 ~ 2.5 orders of magnitude. According to Eq. (4), the coefficient a is related to the permeability of the fracture, and a lower value of a means a higher value of permeability. Therefore, the decrease in the linear coefficient a is caused by dilation of the fracture aperture that increases the fracture permeability. As d increases from 1 mm to 3 mm, the coefficient a significantly decreases, and then the decreasing rate gradually decreases. This conclusion is consistent with the experimental findings in this study (Javadi et al. 2014; Rong et al. 2016 and Yin et al. 2017). The coefficient a increases with an increase in the normal stress. This result is primarily attributed to the closure of the fracture in higher normal stress conditions. Similarly, according to Eq. (4), the decrease in b is attributed to the shear dilation-induced increase in the fracture aperture and a decrease in the flow tortuosity caused by the decrease in the contact area. With the increment of confining stress, the increase in b is ascribed to the closure of the fracture and an increase in the flow path tortuosity as the contact area increases. These phenomena can be verified by the relationship between a and b with d_{dilation}. As shown in Fig. 8 and Fig. 9, both the coefficient a and coefficient b show a decreasing trend with an increase in d_{dilation}. Additionally, the coefficient a shows a decreasing trend with an increase in JRC due to the rougher fractures that cause a larger dilation with the same d. However, the correction between coefficient b and JRC was not established in this study because the variation in coefficient b is controlled by the fracture roughness and fracture aperture. The rougher fracture surfaces cause increases in coefficient b, while the rougher fractures creates a larger aperture during the shear process, which causes a decrease in coefficient b. These two competitive effects produce a trend that was hard to establish for coefficient b and the fracture roughness.

3.2.2 Critical hydraulic gradient analysis

The nonlinear flow effects become more significant in fluid flow in fractures with an increasing flow velocity. The factor E has been used to determine the fluid flow regime (Zeng and Grigg 2006; Zhang and Nemcik 2013; Xia et al. 2016; Liu et al. 2016), which can be written as

$$E = \frac{bQ^2}{aQ+bQ^2} \tag{7}$$

where aQ and bQ^2 are energy losses due to the linear and nonlinear dissipation mechanisms in the fracture, respectively. E denotes the percentage of the nonlinear term that contributes to the ratio of the nonlinear term-induced decrease in the hydraulic gradient to the total decrease in hydraulic gradient. Based on Eq. (3), Q can be solved, written as

$$Q = \frac{aE}{b(1\text{-}E)} \tag{8}$$

The critical hydraulic gradient can be obtained by substituting Eq. (8) into Eq. (3), which is written as follows:

$$J_c = \frac{a^2 E}{b(1\text{-}E)^2} \tag{9}$$

Generally, the critical condition for the transition of linear flow regimes to nonlinear flow regimes has been defined as $E = 0.1$ (Zimmerman et al. 2004; Zhang and Nemcik 2013; Rong et al. 2016). The corresponding J is defined as the critical hydraulic gradient J_c (Liu et al. 2016a; Liu et al. 2016b; Wang et al. 2016). In previous studies of the flow characteristics of fractures, Re has been extensively employed to quantify the nonlinear flow behavior, which can be written as follows (Ranjith and Darlington 2007; Zhang and Nemcik 2013):

$$Re = \frac{\rho Q}{\mu w} \tag{10}$$

In engineering practices, note that rock masses contain hundreds to thousands of fractures, and the Re_c value of each fracture cannot be ascertained. However, the J_c value can be easily obtained. In this study, therefore, J_c was used to evaluate the fracture flow characteristics during shear (Liu et al. 2016a; Wang et al. 2016).

Fig. 10 shows the variation in J_c during shear with different σ_n for four different JRC values. The results show that J_c increases and exhibits two stages as d increases. As d increases from 1 mm to 3 mm, J_c changes significantly, and then the rate of increase gradually decreases. The increase in J_c is mainly attributed to shear-induced dilation. As shown in Fig. 10(e) ~ (h), J_c increases with an increase in $d_{dilation}$. Taking JRC = 5.62 as an example, when $\sigma_n = 0.5$ MPa and the dilation increases from 0.026 mm to 0.504

mm, J_c increases from 0.98 to 3.42 and then increases from 3.42 to 4.36 with an increase in dilation from 0.504 mm to 1.309 mm. This result occurs because the shear dilation causes a distinct change in the fracture geometry and a decrease in the contact ratio, relative roughness and flow tortuosity. These features decrease the inertial losses and generate a large J_c. These results are generally consistent with the work by Yin et al. (2017). In all cases, as σ_n increases, J_c increases. When JRC = 12.16 and d increases from 1 to 9 mm, J_c varies from 0.29 to 1.31 for $\sigma_n = 0.5$ MPa and varies from 0.85 to 2.03 for $\sigma_n = 2.0$ MPa. This is mainly due to the closure of the fracture and increasing contact areas caused by the higher σ_n. According to Eq. (1), Q is proportional to b_h^3; thus, a slight decrease in the fracture aperture causes a large decrease in the flow rate. Therefore, J_c increases with an increase in σ_n. The experimental results also show that the JRC impacts the range of J_c subjected to a certain σ_n. The larger is JRC, the lower is the range of J_c. When $\sigma_n = 1.0$ MPa and d increases from 1 mm to 9 mm, J_c ranges from 1.21 to 8.19 for JRC = 3.21, ranges from 1.16 to 4.7 for JRC = 5.62, ranges from 0.74 to 4.38 for JRC = 7.36, and from 0.45 to 1.65 for JRC = 12.16. According to Schrauf and Evans (1986), the occurrence of nonlinear flow is mainly attributed to the inertial losses due to changes in the flow velocity of the direction along the flow paths. Sharp changes in the fracture aperture along the flow path will promote the variations in the plane velocity due to the acceleration and deceleration of flow to maintain the conservation of mass. This acceleration and deceleration of flow cause deviation from a liner relationship between pressure drop and flow rate (Cornwell and Murphy 1985; Javadi et al. 2014; Wang et al. 2016). Therefore, the nonlinear flow is strongly related to the aperture fields and fracture surface roughness. When shear displacement occurs, the mismatch of the fracture surface causes a relative distribution of the asperities and variable aperture structure (aperture field). The flow path is controlled by the distribution of the aperture field together with the relative distribution of the asperities. As shown in Fig. 2, the rougher fracture trends to generate a wider range of the asperities distribution. This phenomenon indicates that the aperture distribution becomes more anisotropic and heterogeneous for rougher fractures during the shear process, which enhances the local complexity of the flow velocity distributions or direction along the flow channel and enables the fluid flow to more easily become nonlinear. In addition, the dilation of fractures for the same d is larger in the fractures with a larger JRC value. The increase in the fracture aperture yields a lower hydraulic gradient, which is required to obtain the same flow volume. Therefore, a lower value of J_c is obtained for rougher fractures.

3.2.3 Normalized transmissivity

For fluid flow in fractures, transmissivity is an important parameter for estimating the flow characteristics (Zimmerman et al. 2004; Wang et al. 2016). When the flow rate is sufficiently low, the intrinsic transmissivity (T_0) is regarded a constant that is independent of the flow rate. As the flow rate increases, the apparent transmissivity T calculated using Eq. (2) can be applied to assess the nonlinear flow. The normalized transmissivity (T/T_0) is defined as the ratio of the apparent transmissivity to the intrinsic transmissivity, which can be described as a function of Re and the Forchheimer coefficient β as follows (Zimmerman et al. 2004):

$$\frac{T}{T_0} = \frac{1}{1+\beta Re} \tag{11}$$

where T_0 is determined using the best-fit values of the coefficient a.

The relationships between T/T_0 and Re for fractures with different surface roughnesses are shown in Figs. 11 ~ 14. T/T_0 decreases with an increase in Re, which further confirms the deviation of the flow from linearity. For a certain σ_n, as d increases, the transmissivity relationship generally shifts upward. The shift degree of transmissivity increases more significantly for d from 1 mm to 3 mm than from 3 mm to 9 mm. For a certain d, however, the relationship between Re and T/T_0 shifts downward as σ_n increases.

Re_c was determined by establishing the fitting relations in the form of Eq. (9), as shown in Table 3. Note that $T/T_0 = 0.9$ has the same physical meaning as $E = 0.1$, which indicates that the nonlinear term contributes to 10% of the pressure drop. In this case, the corresponding Re is defined as Re_c (Yu.et al. 2017). The range of Re_c is 1.19 to 48.73 for all tested cases, which is the same range reported in the literature (Javadi et al. 2014; Rong et al. 2016).

The values of β for all cases are listed in Table 3. As d increases, β decreases. Taking JRC = 12.16 and $\sigma_n = 1.0$ MPa as an example, with an increase in d from 1 to 9 mm, β decreases from 0.0823 to 0.00407. For a certain d, β generally increases with an increase in σ_n. For JRC = 7.36 at d = 5 mm, β is 0.00456 for $\sigma_n = 0.5$ MPa, 0.00559 for $\sigma_n = 1.0$ MPa, 0.00642 for $\sigma_n = 1.5$ MPa, and 0.00859 for $\sigma_n = 2.0$ MPa. However, the increasing trend was not distinct for d = 1 mm. This phenomenon occurs because the shear contraction at d = 1 mm does not have a clear decreasing trend with an increase in σ_n. It is also observed that β exhibits an increasing trend with an increase in the JRC value. When $\sigma_n = 1.0$ MPa for JRC = 3.21, as d increases from 3 to 9 mm, β decreases from 0.00528 to 0.0025, while for JRC = 12.16, β decreases from 0.01191 to 0.00407.

3.3 Visualization

Visual techniques have the advantage of directly observing the detailed flow behaviors in rough-walled fractures. To provide a better understanding of the effect of the shear process on the nonlinear flow regimes of rough-walled fractures, a visualization shear-flow test was conducted on fracture G3 with a σ_{n} of 0.5 MPa, which is denoted as fracture G3-1 in the following section. For visualization purposes, the upper part of the rock fracture specimen was a transparent replica, and the lower part of the rock fracture specimen was a plaster replica. The physic-mechanical properties of the transparent acrylic material are shown in Table 1. Compared with the plaster material, the transparent acrylic material has a larger value of uniaxial compressive strength and a fairly similar value of elastic modulus. Shear displacement causes degradation of fracture asperities, and different types of materials show different mechanical and deformation behaviors during the shear process. This phenomenon results in the different gouge productions and aperture fields during shear process and influences the fluid flow behaviors in fractures. To avoid the influence of the material property difference on fluid flow behavior, the visualization test was conducted at a small value of normal stress (0.5 MPa). In this condition, the dilation of the transparent specimen is considered to be fairly close to the plaster specimen because no distinct gouge materials are generated during shearing. Since the visualization test mainly focuses on the observation of fluid flow in the fracture during shearing, which is primarily governed by the aperture changes induced by dilation, the acrylic-plaster pair is considered an acceptable replica for studying the channelization characteristics of fractures. Red-dyed water was used to enhance the visibility of the flow paths induced by the shear process, whereas the effect of the shear-induced aperture field distribution and tortuosity on nonlinear flow behavior were not quantitative analyzed due to the limitation of the tracer technique. The visualization test was conducted with a constant water head of 10 cm. This small inlet water head is used to ensure a small value of *Re*; thus, the channelized flow is generated by the shear-induced anisotropic void spaces within the fractures rather than the inertial effects caused by a large water head difference. A high-resolution CCD camera was placed on top of the shear box, which can capture the fluid flow in the fracture in real time. The capture rate was one image per second, which was maintained until the red-dyed water filled the void spaces in the fracture. To maintain a constant starting point of the flow of water into the fracture, the water inlet is set at the bottom of the tank (Fig. 3(b)). In the captured images, the area invaded by the dyed water appears red, and the contact areas were easily distinguished due to their yellow color. Therefore, the binary image method was used to calculate the contact ratio (C) during different shear displacements. A detailed description of this method is provided in Develi and Babadagli 2015.

Images of the fluid flow in fracture G3-1 at different shear displacements are shown in Fig. 15. The channelized flow was observed at all shear steps. When the shear displacement was small (i.e., d = 1 mm), the number of flow paths was larger due to the widely distributed contact area, and the flow pattern was in the form of a network. The dyed water slowly flowed over the entire fracture, which required 105 seconds to fill all void spaces because the rough fracture surfaces may interlock with each other and form a tightly closed fracture with a small aperture at very beginning of shear. As d increases, the number of flow paths decreases due to the shear dilation-induced decrease in the number of contact spots, and the preferential flow channels can be more characteristically observed in the fracture plane. Additionally, the dyed water more quickly reaches the stationary state at a larger shear displacement because the larger aperture decreases the flow resistance. The same visualization test was conducted on another fracture (G3) with a σ_n of 0.5 MPa. The visualization results show that the preferential flow channels are similar, which indicates that the flow paths are repeatable for tests at the same d. The variations in b_h, $d_{dilation}$ and C at different shear displacements are shown in Fig. 16(a). As d increases from 1 to 3 mm, b_h substantially increases. When d ranges from 3 ~ 9 mm, b_h decreases and becomes steadier with an increase in d mainly due to the dilation behavior of the fracture. As shown in Fig. 16(b), the dilation significantly changes and then gradually decreases with an increase in d. Additionally, the increase in $d_{dilation}$ is greater than the b_h. This result shows agreement with the observations of Olsson and Barton (2001). However, the C inversely changes with a change in b_h during shear. As d increases from 1 to 3 mm, C rapidly decreases from 32.9% to 9.27%. When d ranges from 3 ~ 9 mm, the change in C is very small, and a nearly constant value is maintained. The roughness and contact area causes tortuous flow paths, which can cause nonnegligible inertial losses. These features may contribute to nonlinear fluid flow behavior. As shear begins, the flow path is controlled by the relative distribution of the asperities and the distribution of the aperture field. When d is very small (i.e., d = 1 mm), the opposite walls of a rough fracture are slightly mismatched, and a void space with many contact spots forms. At this stage, the roughness of the fracture surface has a dominant role in controlling the fluid flow, and the existing large number of contact areas produce more tortuous flow paths. This phenomenon causes an increase in the degree of the nonlinearity of the fluid flow and decreases in Re_c and J_c. As the shear displacement increases (i.e., d = 1 ~ 3 mm), the rapid increase in fracture aperture causes a rapid decrease in the number of contact areas. Therefore, the influence of the flow tortuosity decreases. These physical processes cause considerable increases in both Re_c and J_c. With a continuous increase in d to 9 mm, the variation in C is very small, and a nearly constant value is maintained. Therefore, the effect of the contact-induced flow path tortuosity on nonlinear flow is not the key factor. The influence of the fracture surface roughness on the nonlinear flow decreases, and the shear dilation-induced increase in fracture aperture plays a dominant role in controlling the nonlinear flow behavior, which causes gradual increases in Re_c and J_c.

4. Conclusions

1) Forchheimer's law can well describe the nonlinear flow in rough-walled fractures during shear at different normal stresses. Both the linear coefficient a and the nonlinear coefficient b decrease as the shear dilation increases. The degrees of the decreases in the two coefficients at the shear displacement of 1 to 3 mm are more significant than that for the shear displacement of 3 to 9 mm. The decrease in a as d increased from 1 to 9 mm was approximately 0.5 ~ 1.0 orders of magnitude, and the decrease in b was approximately 2.0 ~ 2.5 orders of magnitude. The coefficients a and b are very sensitive to the normal stress. Both a and b decrease with an increase in the normal stress.
2) With an increase in shear dilation, the critical hydraulic gradient increases in two different stages. As the shear displacement increases from 1 mm to 3 mm, the critical hydraulic gradient significantly changes, and the rate of increase then gradually decreases with an increase in the shear displacement. As normal

stress increases, the critical hydraulic gradient increases due to the fracture closure. In addition, the critical hydraulic gradient is influenced by the roughness of the fracture surfaces. With an increase in the fracture surface roughness, the critical hydraulic gradient decreases.

3) The normalized transmissivity, which is a function of the hydraulic gradient, is analyzed. As the shear displacement increases, the fitted curves shift upward and then downward with an increase in normal load. The coefficient β decreases with an increase in shear displacement but increases with an increase in normal load. The value of β increases with an increase in fracture surface roughness.

4) The visualization tests show that channelized flow occurs in all cases. When the shear displacement is small, the number of flow paths is large due to the distribution of the contact areas, and the dyed water slowly flows over the entire fracture. With an increase in shear displacement, the shear dilation-induced increase in fracture aperture causes the contact ratio to rapidly decreases to a small value and then maintain an approximately constant value. The flow paths are focused in the void spaces with relatively large apertures, in which some preferential flow channels form. Channels with larger apertures have lower flow resistance, and the dyed water can reach the stationary state faster with an increase in shear displacement.

In this study, we investigated the effect of shear on the nonlinearity of fluid flow in single rough-walled rock fractures. However, more in-depth research of this issue is required. In future studies, we will focus on the effects of the fracture surface roughness and shear behavior on the nonlinear flow regime in complex fracture networks.

Acknowledgments

This study has been partially funded by National Natural Science Foundation of China (Grant Nos. 51979272 and 51709260), Natural Science Foundation of Jiangsu Province, China (Grant No. BK20170276), JSPS-NSFC Bilateral Joint Research Project (Grant No. 51611140122) and China Scholarship Council (CSC NO. 201608370099). These supports are gratefully acknowledged.

Conflict of Interest

The authors declare that they have no conflict of interest.

References

Adler PM, Malevich AE, Mityushev VV. Nonlinear correction to Darcy’s law for channels with wavy walls. Acta Mechanica, 2013, 224(8):1823-1848.

Brown S R. Fluid flow through rock joints: The effect of surface roughness. Journal of Geophysical Research Solid Earth, 1987, 92(B2):1337-1347.

Brown S R, Stockman H W, Reeves S J. Applicability of the Reynolds Equation for modeling fluid flow between rough surfaces. Geophysical Research Letters, 1995, 22(18):2537-2540.

Brush DJ, Thomson NR. Fluid flow in synthetic rough-walled fractures: Navier-Stokes, Stokes, and local cubic law simulations. Water Resources Research, 2011, 39(4):1037-1041.

Babadagli T, Ren XJ, Develi K. Effects of fractal surface roughness and lithology on single and multiphase flow in a single fracture: an experimental investigation.

International Journal of Multiphase Flow. 2015, 68:40–58.

Chen YD, Liang WG, Lian HJ, Yang JF, Nguyen VP. Experimental study on the effect of fracture geometric characteristics on the permeability in deformable rough-walled fractures. International Journal of Rock Mechanics & Mining Sciences, 2017, 98:121-140.

Chen YF, Hu SH, Hu R, Zhou CB. Estimating hydraulic conductivity of fractured rocks from high‐pressure packer tests with an Izbash's law‐based empirical model. Water Resources Research, 2015, 51(4):2096-2118.

Cherubini C, Giasi CI, Pastore N. Bench scale laboratory tests to analyze non-linear flow in fractured media. Hydrology & Earth System Sciences Discussions, 2012, 9(4):2511-2522.

Chen Z, Narayan SP, Yang Z, Rahman SS. An experimental investigation of hydraulic behaviour of fractures and joints in granitic rock. International Journal of Rock Mechanics & Mining Sciences 2000; 37:1061–71.

Cornwell, D.K, Murphy, et al. Experiments with non-Darcy flow in joints with large scale roughness. Inetenational Symposium on Fundamentals of Rock Joints, 1985, Centek, Lulea.

Develi K, Babadagli T. Experimental and visual analysis of single-phase flow through rough fracture replicas. International Journal of Rock Mechanics & Mining Sciences, 2015, 73:139-155.

Esaki T, Du S, Mitani Y, Ikusada, Jing L. Development of shear-flow test apparatus and determination of coupled properties for a single rock joint. International Journal of Rock Mechanics & Mining Sciences, 1999, 36(5):641-650.

Huang N, Liu R, Jiang Y. Numerical study of the geometrical and hydraulic characteristics of 3D self-affine rough fractures during shear. Journal of Natural Gas Science & Engineering, 2017, 45.

Javadi M, Sharifzadeh M, Shahriar K. A new geometrical model for non-linear fluid flow through rough fractures. Journal of Hydrology, 2010, 389(1):18-30.

Javadi M, Sharifzadeh M, Shahriar K, Mitani Y. Critical Reynolds number for nonlinear flow through rough-walled fractures: The role of shear processes. Water Resources Research, 2014, 50(2):1789–1804.

Kosakowski G, Berkowitz B. Flow pattern variability in natural fracture intersections. Geophysical Research Letters, 1999, 26(12):1765–1768.

Koyama T, Li B, Jiang YJ, Jing LR. Coupled shear-flow tests for rock fractures with visualization of the fluid flow and their numerical simulations. International Journal of Geotechnical Engineering, 2012, 2(3):215-227.

Koyama T, Neretnieks I, Jing L. A numerical study on differences in using Navier–Stokes and Reynolds equations for modeling the fluid flow and particle transport in single rock fractures with shear. International Journal of Rock Mechanics & Mining Sciences, 2008, 45(7):1082-1101.

Li B, Jiang YJ, Koyama T, Jing LR. Experimental study of the hydro-mechanical behavior of rock joints using a parallel-plate model containing contact areas and artificial fractures. International Journal of Rock Mechanics & Mining Sciences, 2008, 45(3):362-375.

Li B, Liu R, Jiang Y J. Influences of hydraulic gradient, surface roughness, intersecting angle, and scale effect on nonlinear flow behavior at single fracture intersections. Journal of Hydrology, 2016, 538(538):440-453.

Leung CTO, Zimmerman RW. Estimating the Hydraulic Conductivity of

Two-Dimensional Fracture Networks Using Network Geometric Properties. Transport in Porous Media, 2012, 93(3):777-797.

Liu JS, Chen ZW, Elsworth D, Qu HY, Chen D. Interactions of multiple processes during CBM extraction: A critical review. International Journal of Coal Geology, 2011, 87(3):175-189.

Liu RC, Li B, Jiang YJ. Critical hydraulic gradient for nonlinear flow through rock fracture networks: The roles of aperture, surface roughness, and number of intersections. Advances in Water Resources, 2016a, 88:53-65.

Liu RC, Li B, Jiang YJ, Huang N. Review: Mathematical expressions for estimating equivalent permeability of rock fracture networks. Hydrogeology Journal, 2016c, 24(7):1-27.

Liu RC, Yu LY, Jiang YJ. Quantitative Estimates of Normalized Transmissivity and the Onset of Nonlinear Fluid Flow Through Rough Rock Fractures. Rock Mechanics & Rock Engineering, 2016b, 50(4):1-9.

Moutsopoulos KN. Exact and approximate analytical solutions for unsteady fully developed turbulent flow in porous media and fractures for time dependent boundary conditions. Journal of Hydrology, 2009, 369(1):78-89.

Olsson R, Barton N. An improved model for hydromechanical coupling during shearing of rock joints. International Journal of Rock Mechanics & Mining Sciences, 2001, 38(3):317-329.

Oron A P, Berkowitz B. Flow in rock fractures: The local cubic law assumption reexamined. Water Resources Research, 1998, 34(11): 2811-2825.

Qian J, Zhan H, Chen Z, Ye H. Experimental study of solute transport under non-Darcian flow in a single fracture. Journal of Hydrology, 2011, 399(3):246-254.

Ranjith PG, Darlington W. Nonlinear single‐phase flow in real rock joints. Water Resources Research, 2007, 43(9):146-156.

Rong G, Hou D, Yang J, Cheng L, Zhou CB. Experimental study of flow characteristics in non-mated rock fractures considering 3D definition of fracture surfaces. Engineering Geology, 2017, 220:152-163.

Rong G, Yang J, Cheng L, Zhou CB. Laboratory investigation of nonlinear flow characteristics in rough fractures during shear process. Journal of Hydrology, 2016, 541:1385-1394.

Schrauf TW, Evans DD. Laboratory studies of gas flow through a single natural fracture. Water Resources Research, 1986, 22(7):1038-1050.

Tse R, Cruden D M. Estimating joint roughness coefficients. International Journal of Rock Mechanics & Mining Sciences & Geomechanics Abstracts, 1979, 16(5):303-307.

Tzelepis V, Moutsopoulos K N, Papaspyros J N E, Tsihrintzis V A. Experimental investigation of flow behavior in smooth and rough artificial fractures. Journal of Hydrology, 2015, 521(2):108-118.

Wang CG, Liu JS, Feng JL, Wei MY, Wang CC, Jiang YJ. Effects of Gas Diffusion from Fractures to Coal Matrix on the Evolution of Coal Strains: Experimental Observations. International Journal of Coal Geology, 2016, 162:74-84.

Wang CG, Zhai PC, Chen ZW, Liu JS, Wang LS, Xie J. Experimental Study of Coal Matrix-fracture Interaction under Constant Volume Boundary Condition. International Journal of Coal Geology, 2017,181,124-132.

Wang L, Cardenas MB, Slottke DT, Ketcham RA, Sharp JM. Modification of the Local Cubic Law of fracture flow for weak inertia, tortuosity, and roughness. Water Resources Research, 2015, 51(4):2064-2080.

Wang M, Chen YF, Ma GW, Zhou JQ, Zhou CB. Influence of surface roughness on nonlinear flow behaviors in 3D self-affine rough fractures: Lattice Boltzmann simulations. Advances in Water Resources, 2016, 96:373-388.

Wei W, Xia Y. Geometrical, fractal and hydraulic properties of fractured reservoirs: A mini-review. Adv. Geo Energy, 2017, 1(1): 31-38.

Wu Y, Liu JS, Chen ZW, Elsworth D， Pone D. A dual poroelastic model for CO_2-enhanced coalbed methane recovery. International Journal of Coal Geology, 2011, 86(2-3): 177-189.

Xia CC, Qian X, Lin P, Xiao WM, Gui Y. Experimental Investigation of Nonlinear Flow Characteristics of Real Rock Joints under Different Contact Conditions. Journal of Hydraulic Engineering, 2016, 143(3).

Xiong XB, Li B, Jiang YJ, Koyama T, Zhang CH. Experimental and numerical study of the geometrical and hydraulic characteristics of a single rock fracture during shear. International Journal of Rock Mechanics & Mining Sciences, 2011, 48(8):1292-1302.

Yeo I W, De Freitas, M H, Zimmerman R W. Effect of shear displacement on the aperture and permeability of a rock fracture. International Journal of Rock Mechanics & Mining Sciences, 1998, 35(8), 1051–1070.

Yin Q, Jing HW, Liu RC, Ma GW, Yu LY, Su HJ. Experimental Study on Stress-Dependent Nonlinear Flow Behavior and Normalized Transmissivity of Real Rock Fracture Networks. Geofluids, 2018.

Yin Q, Ma GW, Jing HW, Wang HD, Su HJ, Wang YC, Liu RC. Hydraulic properties of 3D rough-walled fractures during shearing: an experimental study. Journal of Hydrology, 2017, 555.

Yu LY, Liu RC, Jiang YJ. A Review of Critical Conditions for the Onset of Nonlinear

Fluid Flow in Rock Fractures. Geofluids, 2017.

Zeng Z, Grigg R. A Criterion for Non-Darcy Flow in Porous Media. Transport in Porous Media, 2006, 63(1):57-69.

Zhang W, Dai B, Liu Z, Zhou C. A pore-scale numerical model for non-Darcy fluid flow through rough-walled fractures. Computers & Geotechnics, 2017, 87:139-148.

Zhang ZY, Nemcik J. Fluid flow regimes and nonlinear flow characteristics in deformable rock fractures. Journal of Hydrology, 2013, 477(1):139-151.

Zhou JQ, Hu SH, Fang S, Chen YF, Zhou CB. Nonlinear flow behavior at low Reynolds numbers through rough-walled fractures subjected to normal compressive loading. International Journal of Rock Mechanics & Mining Sciences. 2015, 80:202–218.

Zimmerman RW, Al-Yaarubi A, Pain CC, Grattoni CA. Non-linear regimes of fluid flow in rock fractures. International Journal of Rock Mechanics & Mining Sciences, 2004, 41(3):384.

Zimmerman RW, Bodvarsson G S. Hydraulic conductivity of rock fractures. Transport in Porous Media, 1996, 23(1):1-30.

Table 1 Physico-mechanical properties of plaster and acrylic specimen

Physico-mechanical properities	Index	Unit	Plaster specimen	Acrylic specimen
Density	ρ	g/cm^3	2.066	1.192
Compressive strength	σ_c	MPa	38.5	91
Modulus of elasticity	E_s	MPa	28700	24744
Poisson's ratio	v	–	0.23	0.19
Tensile strength	σ_t	MPa	2.5	5.6
Cohesion	c	MPa	5.3	19.9
Internal friction angle	φ	°	60	42.8

Table 2 Experimental results of the characteristic mechanical parameter during shear flow tests

Specimen N0.	Case NO.	JRC	σ_n (MPa)	d_{peak} (mm)	τ_{peak} (MPa)	K_s (MPa/mm)	d_{normal} (mm)	d_{contra} (mm)
G1	G1-1	3.21	0.5	0.844	0.515	0.61	1.080	-0.063
	G1-2		1.0	1.167	1.003	0.86	0.850	-0.080
	G1-3		1.5	1.244	1.407	1.13	0.687	-0.118
	G1-4		2.0	1.417	1.789	1.26	0.561	-0.173
G2	G2-1	5.62	0.5	0.878	0.652	0.74	1.309	-0.003
	G2-2		1.0	1.034	1.136	1.10	1.235	-0.042
	G2-3		1.5	1.195	1.497	1.25	1.09	-0.063
	G2-4		2.0	1.228	1.834	1.49	0.919	-0.073
G3	G3-1	7.36	0.5	0.94	0.770	0.82	1.835	-0.007
	G3-2		1.0	1.059	1.204	1.14	1.212	-0.032
	G3-3		1.5	1.098	1.536	1.40	0.999	-0.060
	G3-4		2.0	1.141	2.070	1.80	0.956	-0.143
G4	G4-1	12.16	0.5	0.892	0.813	0.91	2.472	-0.013
	G4-2		1.0	1.074	1.485	1.40	2.200	-0.064
	G4-3		1.5	1.152	1.872	1.63	1.685	-0.074
	G4-4		2.0	1.168	2.141	1.83	1.269	-0.073

Table 3 Measured results of J_c , Re_c and β for different roughness fractures during shear

Specime N0.	σ_n (MPa)	d (mm)	J_c	Re_c	β	Specime N0.	σ_n (MPa)	d (mm)	J_c	Re_c	β
G1-1	0.5	1	1.154	1.83	0.06051	G3-1	0.5	1	0.496	1.40	0.07916
		3	4.481	21.16	0.00520			3	2.327	15.74	0.00706
		5	5.798	30.11	0.00367			5	2.573	24.37	0.00456
		7	6.567	40.40	0.00275			7	2.894	29.16	0.00381
		9	6.934	48.73	0.00227			9	3.048	39.12	0.00284
G1-2	1.0	1	1.208	1.52	0.07298	G3-2	1.0	1	0.736	1.19	0.09322
		3	6.701	19.56	0.00568			3	2.859	13.27	0.00837
		5	7.322	28.13	0.00395			5	3.627	19.87	0.00559
		7	7.764	35.05	0.00317			7	3.989	24.00	0.00463
		9	8.187	44.44	0.00250			9	4.379	30.28	0.00367
G1-3	1.5	1	1.483	1.65	0.06710	G3-3	1.5	1	0.957	1.24	0.08930
		3	7.331	17.44	0.00637			3	3.339	11.78	0.00943
		5	7.733	25.90	0.00429			5	3.836	17.31	0.00642
		7	8.182	30.69	0.00362			7	4.499	21.57	0.00515
		9	8.493	38.85	0.00286			9	4.659	29.55	0.00376
G1-4	2.0	1	1.501	1.52	0.07311	G3-4	2.0	1	1.216	1.25	0.08909
		3	8.578	16.53	0.00672			3	3.926	10.17	0.01092
		5	8.712	24.91	0.00446			5	4.296	12.93	0.00859
		7	9.335	28.93	0.00384			7	4.978	18.24	0.00609
		9	9.592	38.75	0.00274			9	5.073	26.27	0.00423
G2-1	0.5	1	0.979	1.56	0.07117	G4-1	0.5	1	0.289	1.27	0.08733
		3	3.417	16.20	0.00686			3	0.982	12.23	0.00908
		5	3.873	21.45	0.00518			5	1.126	18.89	0.00588
		7	4.113	27.57	0.00403			7	1.266	24.47	0.00454
		9	4.356	35.27	0.00315			9	1.312	29.71	0.00374
G2-2	1.0	1	1.156	1.48	0.07520	G4-2	1.0	1	0.448	1.34	0.08287
		3	3.579	13.65	0.00814			3	1.010	9.33	0.01191
		5	4.276	23.89	0.00465			5	1.352	16.93	0.00656
		7	4.490	27.23	0.00408			7	1.588	23.15	0.0048
		9	4.698	32.21	0.00345			9	1.651	27.3	0.00407
G2-3	1.5	1	1.257	1.35	0.08235	G4-3	1.5	1	0.580	1.28	0.08711
		3	4.286	13.45	0.00826			3	1.194	8.10	0.01371
		5	4.728	21.66	0.00513			5	1.599	14.81	0.0075

		7	4.828	25.37	0.00438			7	1.805	21.83	0.00509
		9	5.006	29.71	0.00374			9	1.959	24.05	0.00462
G2-4	2.0	1	1.312	1.27	0.08717	G4-4	2.0	1	0.846	1.15	0.09651
		3	4.796	12.55	0.00885			3	1.500	8.24	0.01347
		5	5.086	20.39	0.00545			5	1.735	13.4	0.00829
		7	5.211	24.86	0.00447			7	1.930	19.7	0.00564
		9	5.391	28.06	0.00396			9	2.028	23.1	0.00481

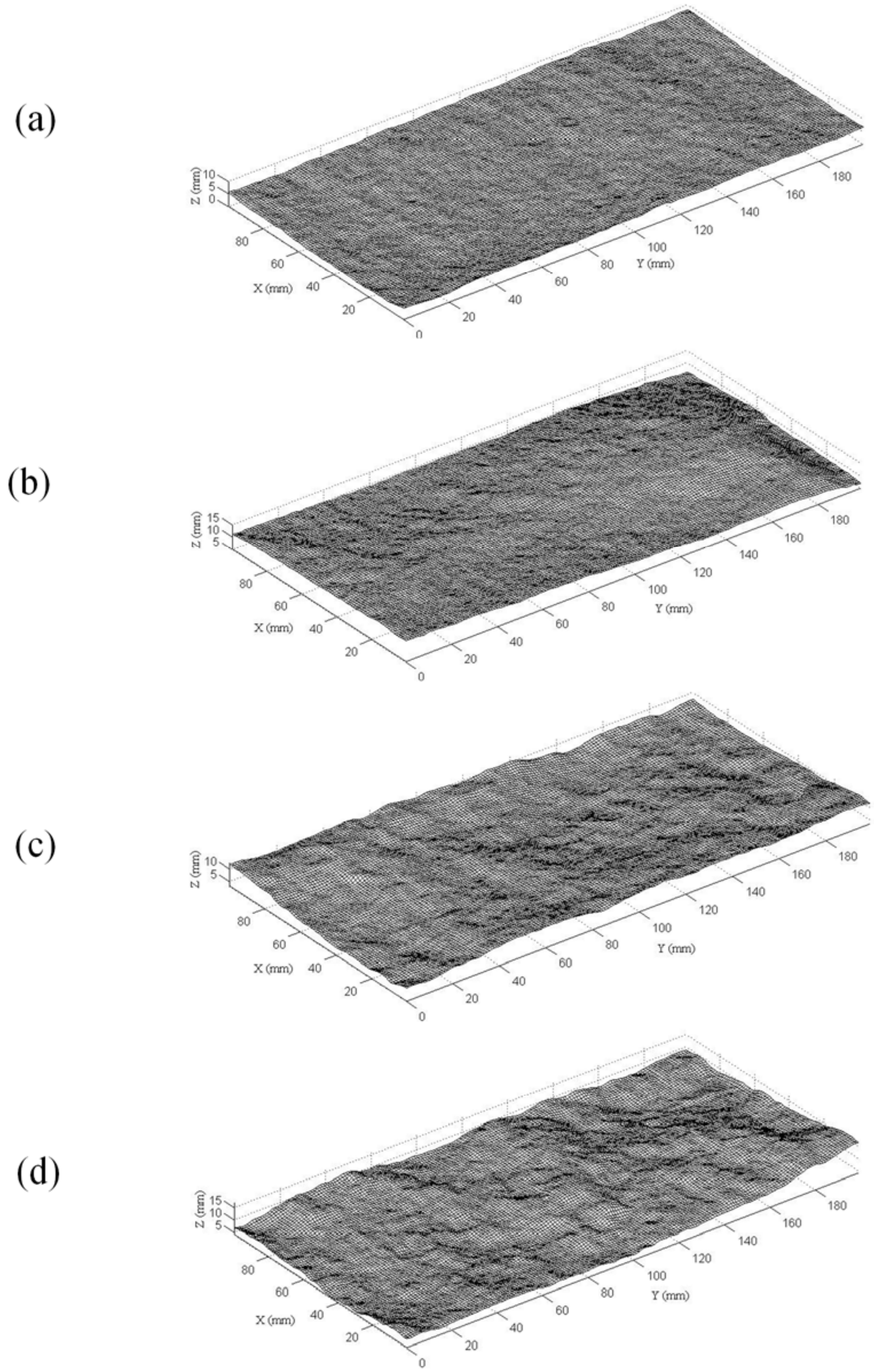

Fig. 1 Scanning graphs of four fracture surface: (a) Specimen G1, JRC = 3.21; (b) specimen G2, JRC = 5.62; (c) specimen G3, JRC = 7.36; and (d) specimen G4, JRC = 12.16.

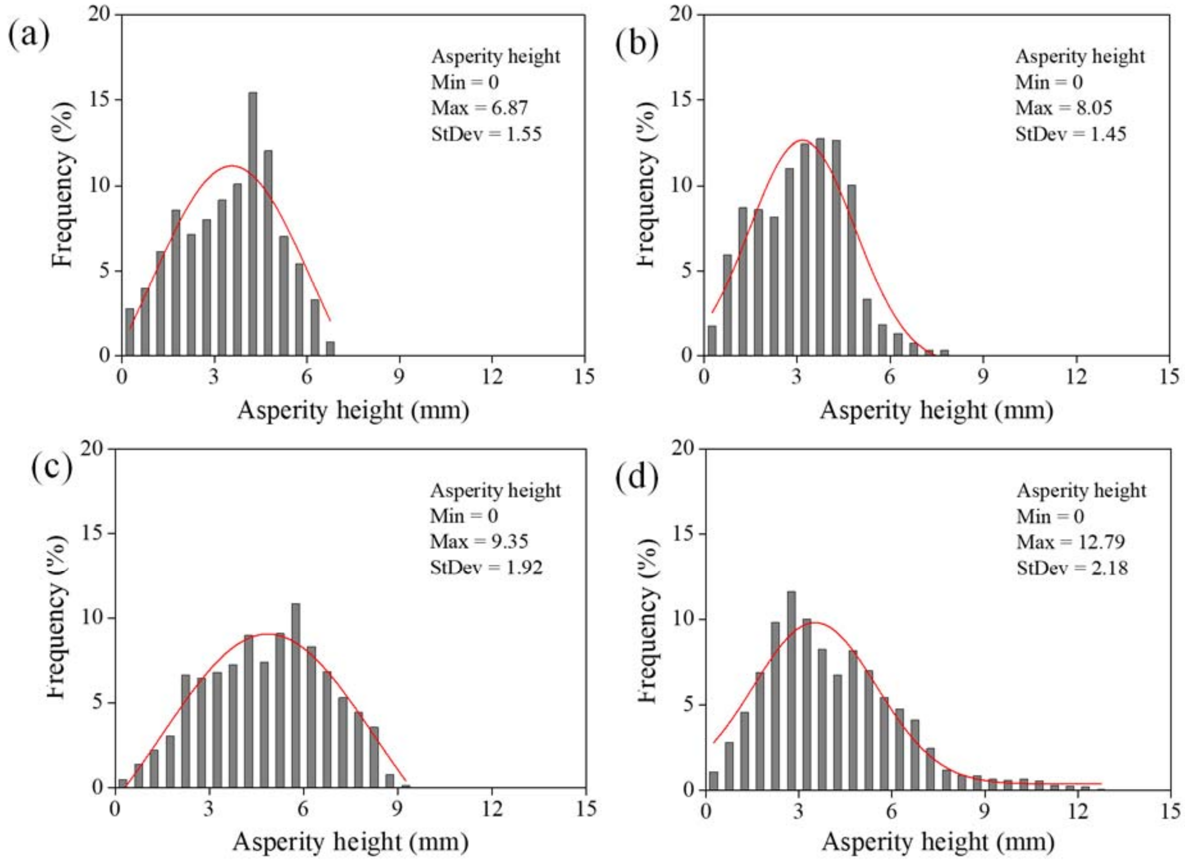

Fig. 2 Frequency versus asperity height of four fracture surfaces: (a) for fracture G1; (b) for fracture G2; (c) for fracture G3; and (d) for fracture G4.

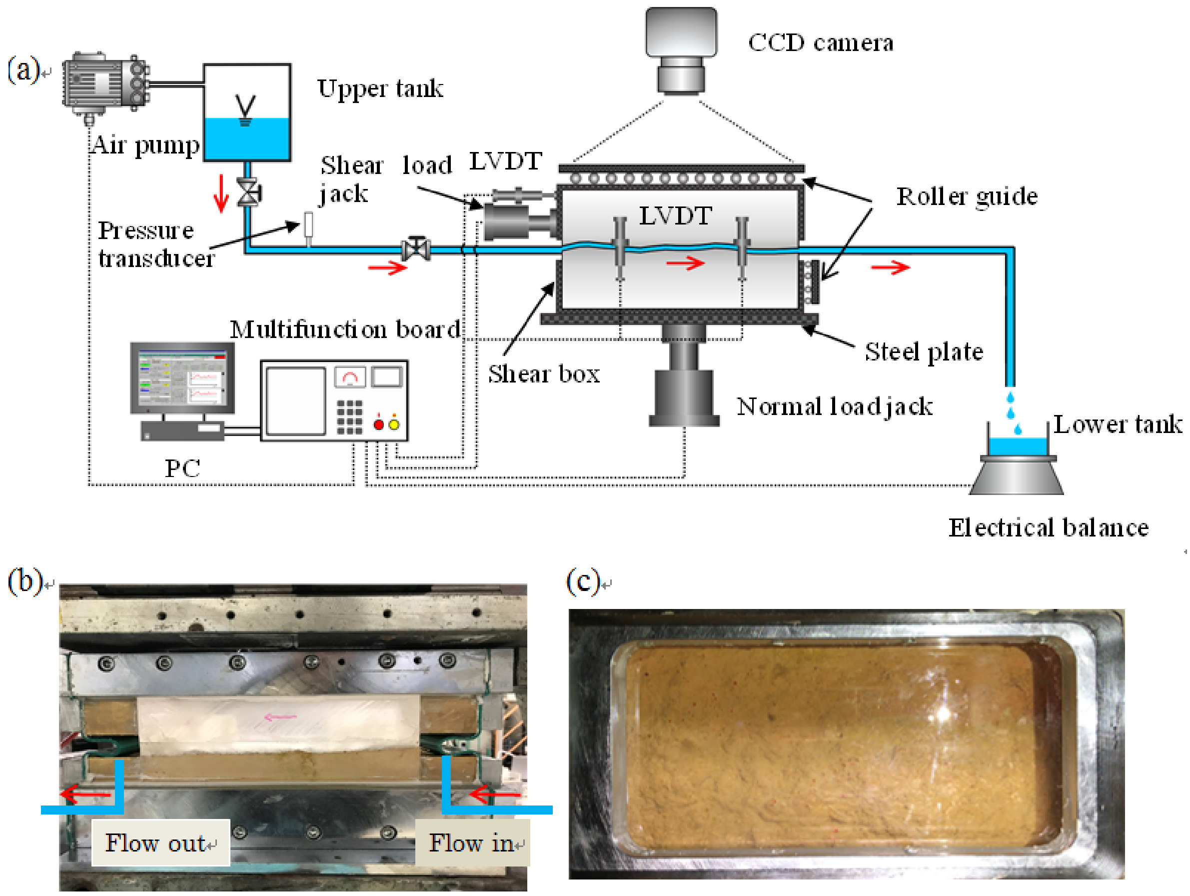

Fig. 3 Schematic view of the coupled shear-flow test apparatus (arrow represents water flow direction). (a) Hydraulic testing system; (b) Side view of the shear box; and (c) Top view of shear box.

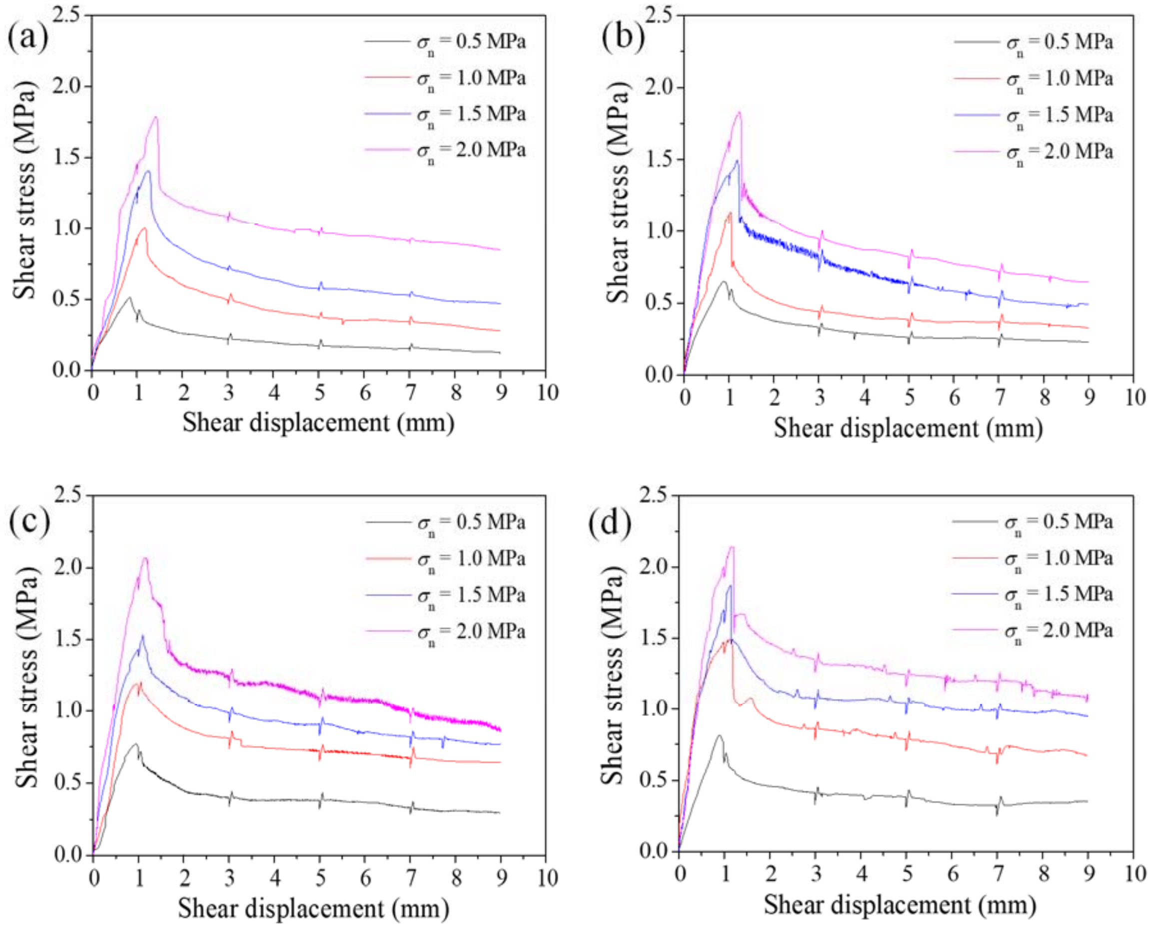

Fig. 4 Shear stress versus shear displacement of fracture specimens under different normal stresses: (a) for fracture G1; (b) for fracture G2; (c) for fracture G3 and (d) for fracture G4.

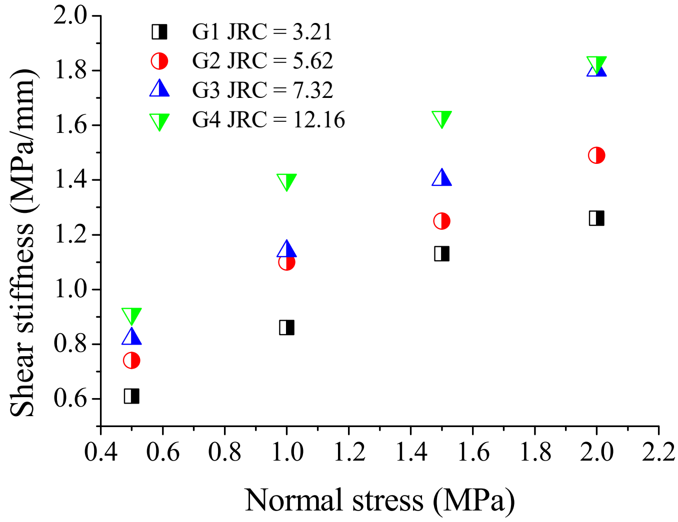

Fig. 5 Relationship between shear stiffness and normal stress of different fracture specimens

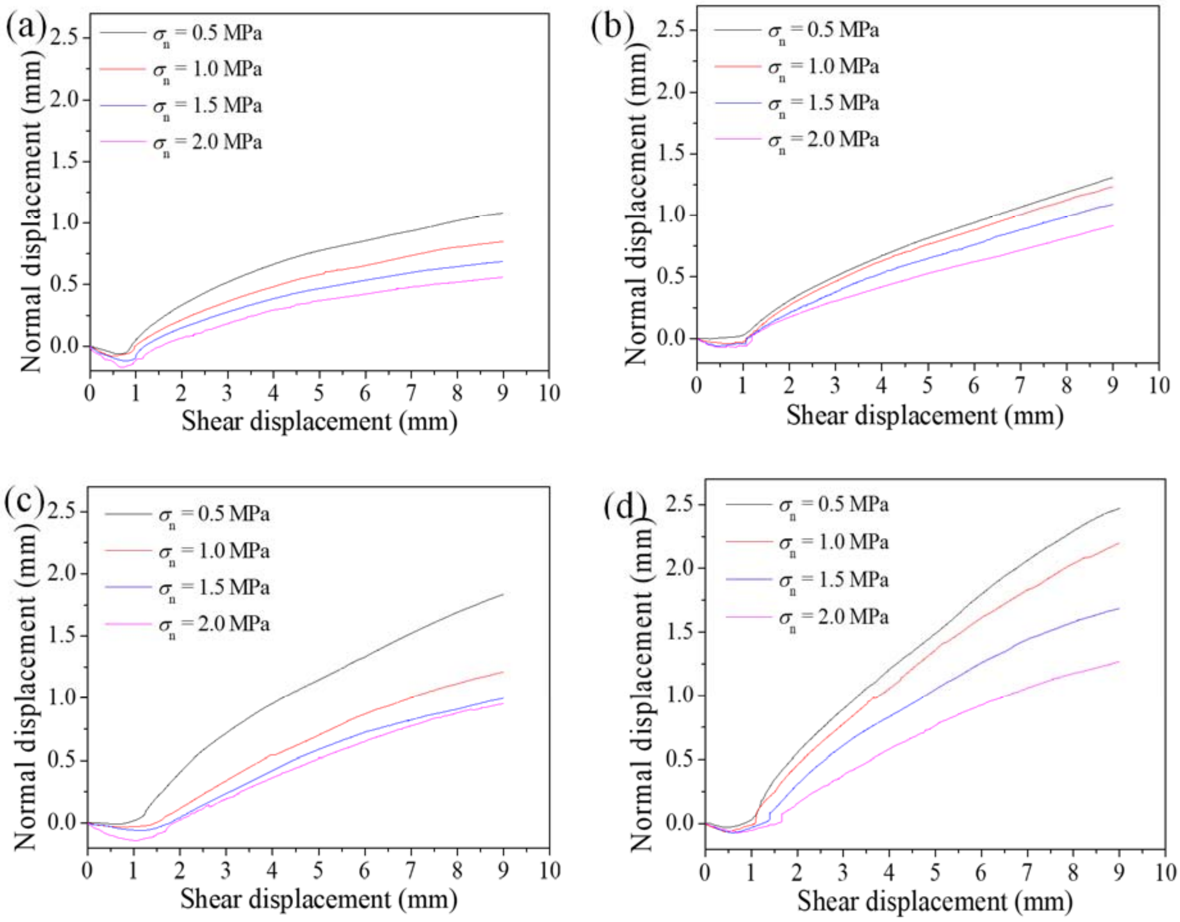

Fig. 6 Normal displacement versus shear displacement of fracture specimens under different normal stresses: (a) for fracture G1; (b) for fracture G2; (c) for fracture G3 and (d) for fracture G4.

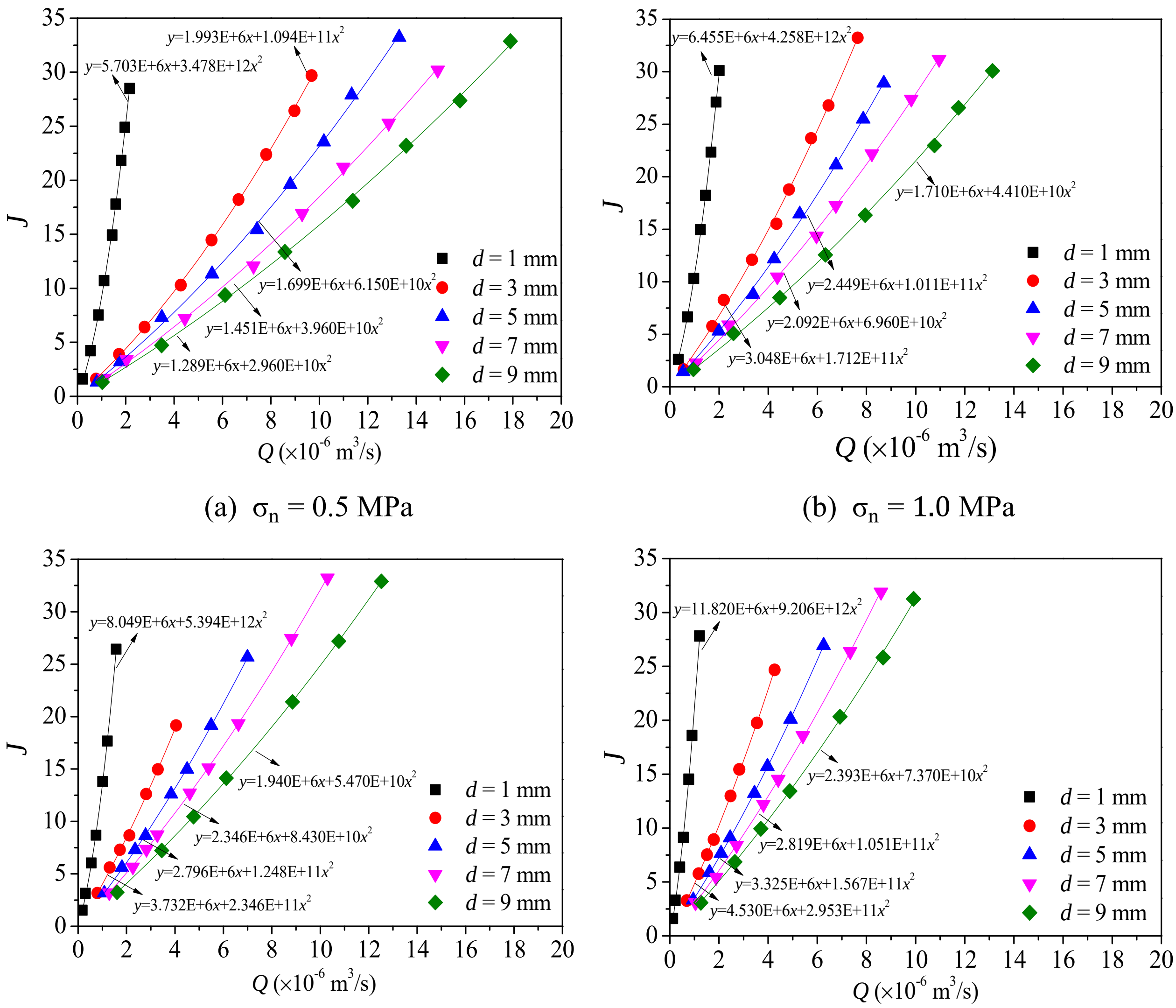

(a) σ_n = 0.5 MPa (b) σ_n = 1.0 MPa

(c) σ_n = 1.5 MPa (d) σ_n = 2.0 MPa

Fig. 7 Relationships between hydraulic gradient (J) and volumetric flow rate (Q) for G1 under different normal stresses.

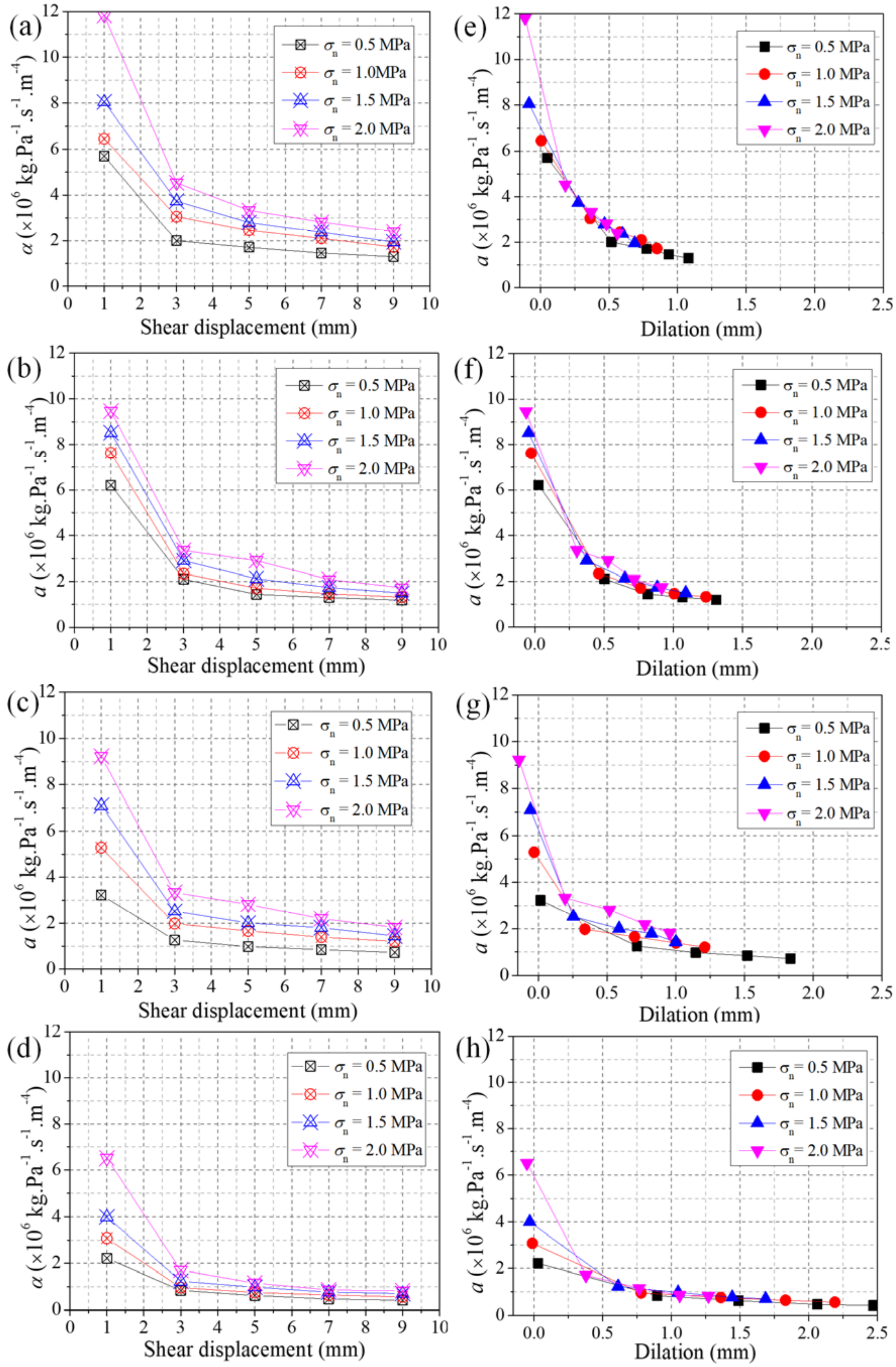

Fig. 8 Relationships between linear coefficient *a* and shear displacement: (a) G1, (b) G2, (c) G3, and (d) G4. Relationships between linear coefficient *a* and dilation: (e) G1, (f) G2, (g) G3, and (h) G4.

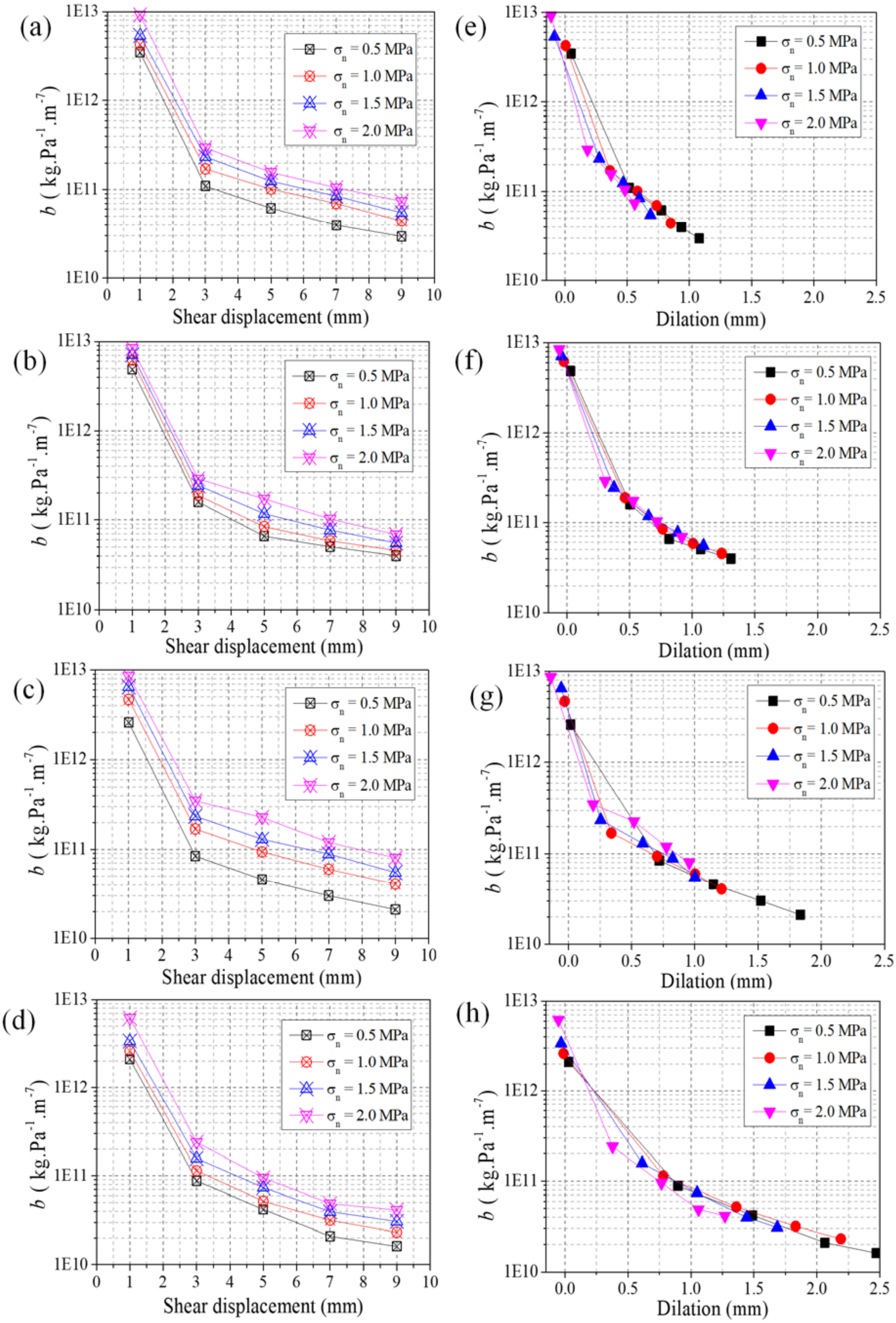

Fig. 9 Relationships between linear coefficient *b* and shear displacement: (a) G1, (b) G2, (c) G3, and (d) G4. Relationships between linear coefficient *b* and dilation: (e) G1, (f) G2, (g) G3, and (h) G4.

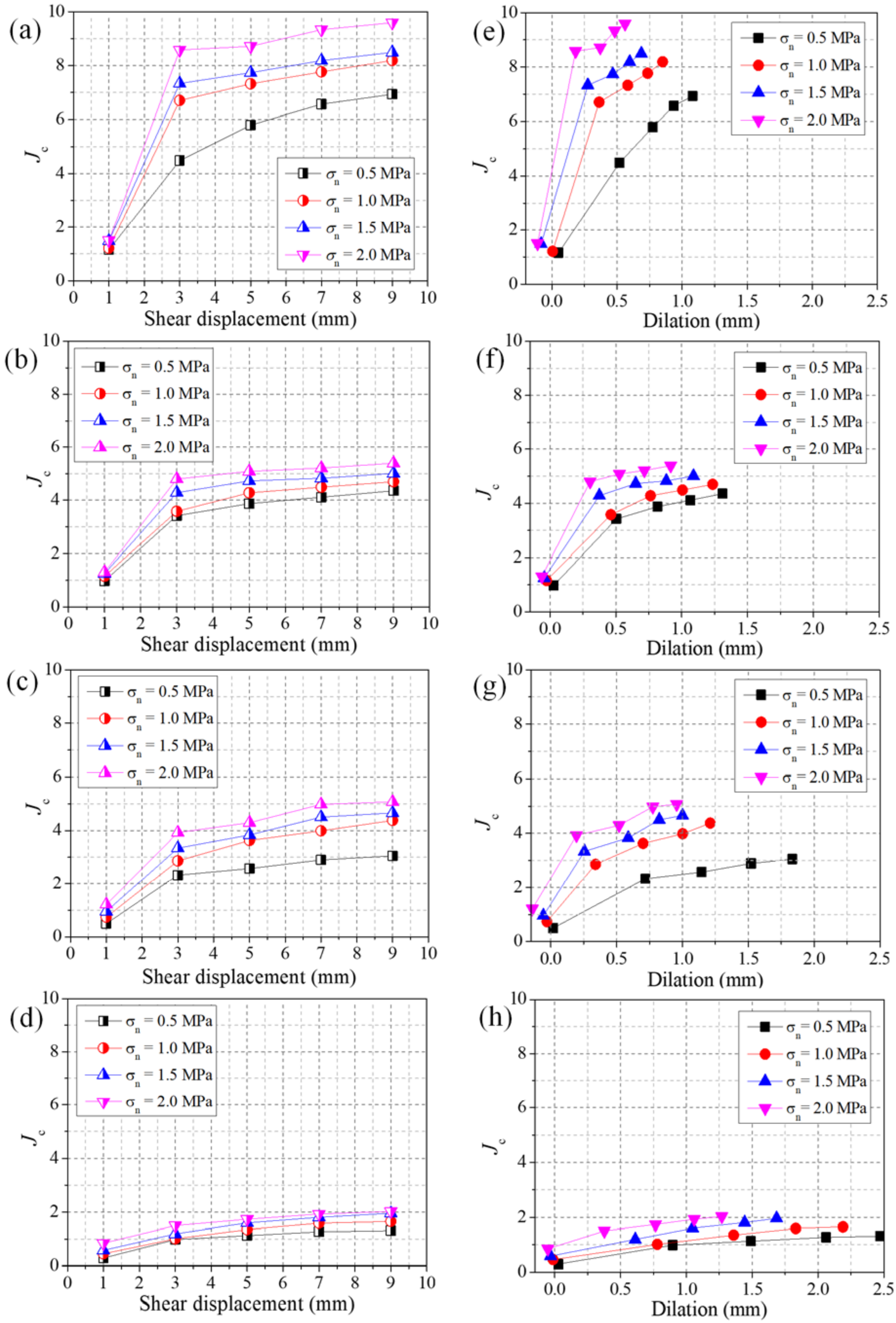

Fig. 10 Relationships between critical hydraulic gradient J_c and shear displacement d: (a) G1, (b) G2, (c) G3, and (d) G4. Relationships between critical hydraulic gradient J_c and dilation: (e) G1, (f) G2, (g) G3, and (h) G4.

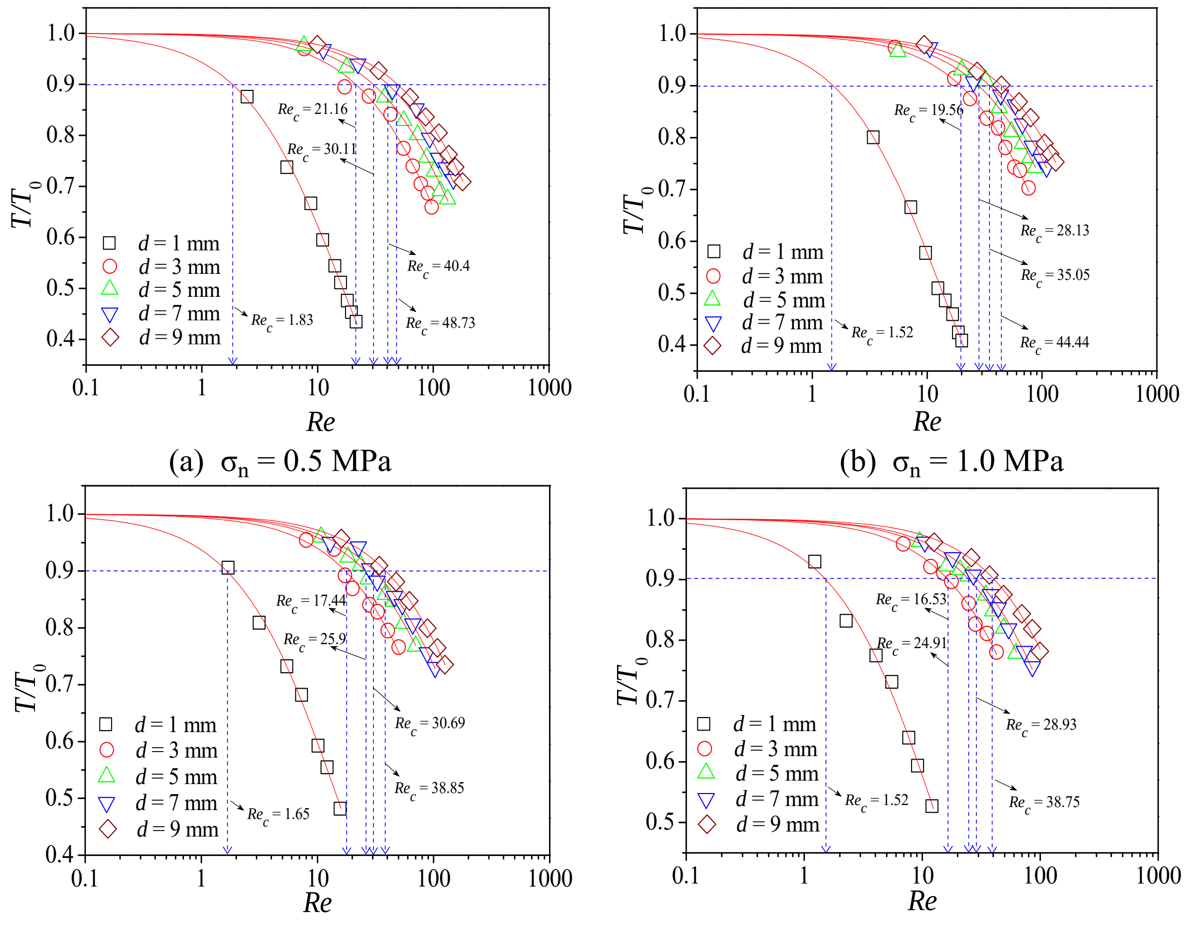

(a) σ_n = 0.5 MPa (b) σ_n = 1.0 MPa

(c) σ_n = 1.5 MPa (d) σ_n = 2.0 MPa

Fig. 11 Relationships between normalized transmissivity (T/T_0) and Reynolds number (*Re*) for G1 under different normal stresses.

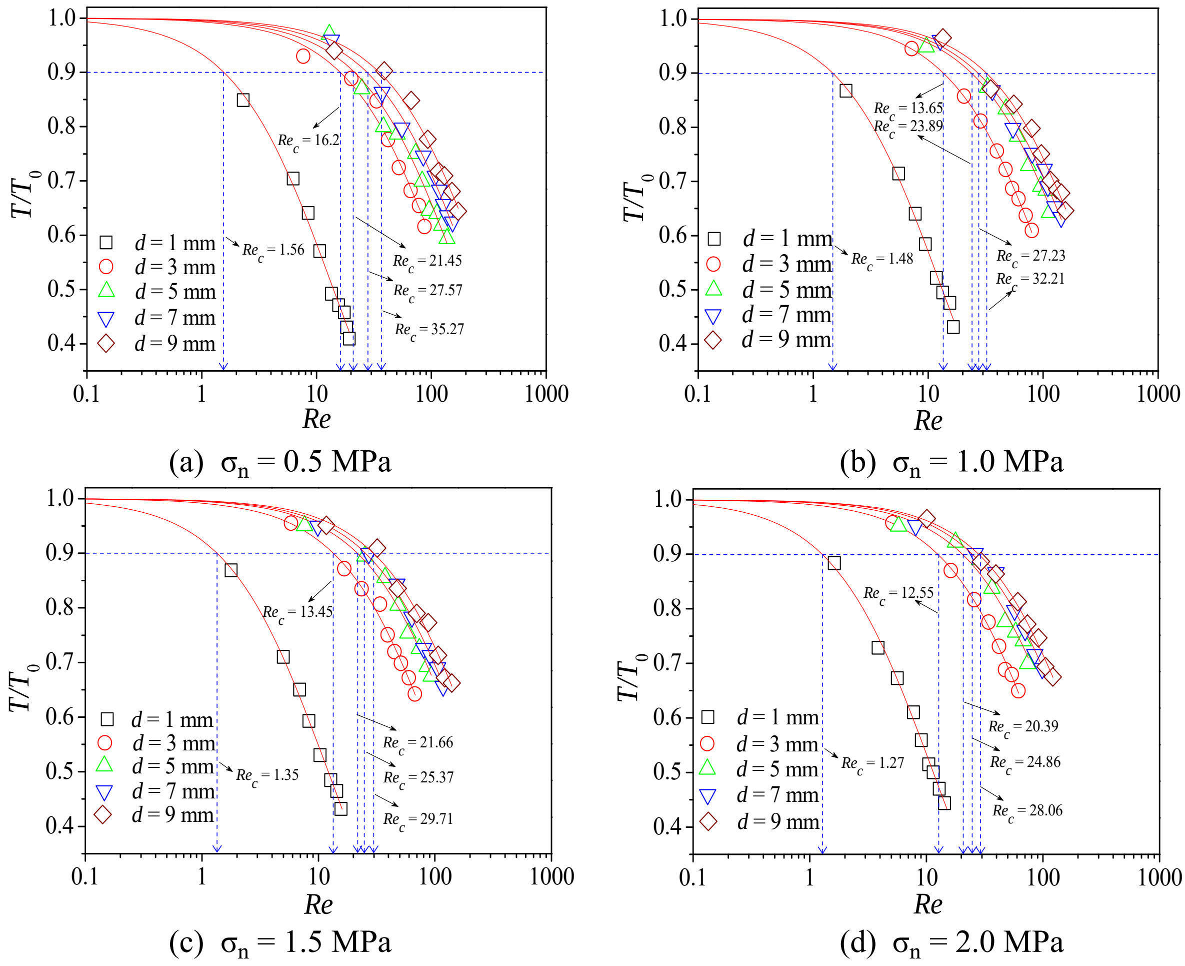

Fig. 12 Relationships between normalized transmissivity (T/T_0) and Reynolds number (*Re*) for G2 under different normal stresses.

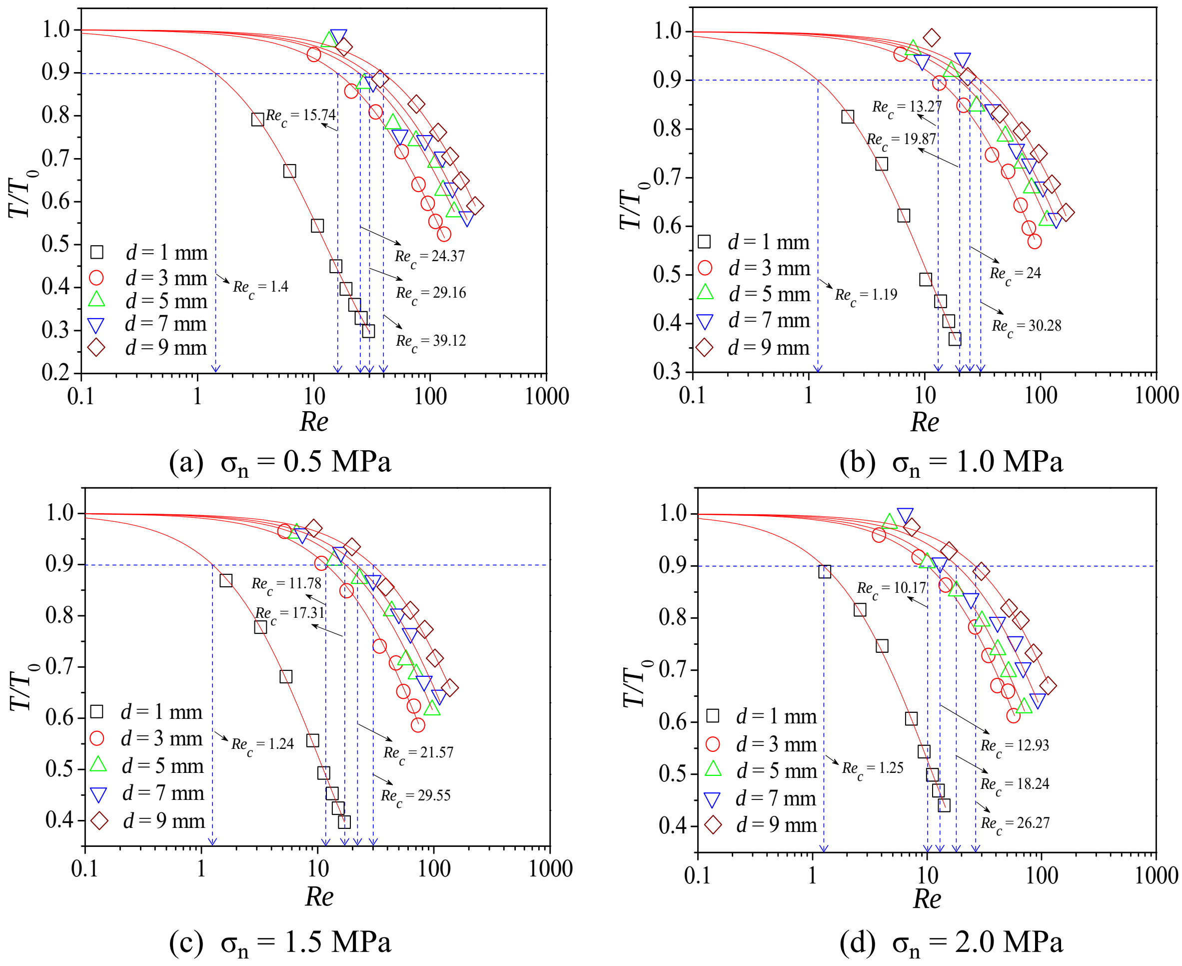

Fig. 13 Relationships between normalized transmissivity (T/T_0) and Reynolds number (Re) for G3 under different normal stresses.

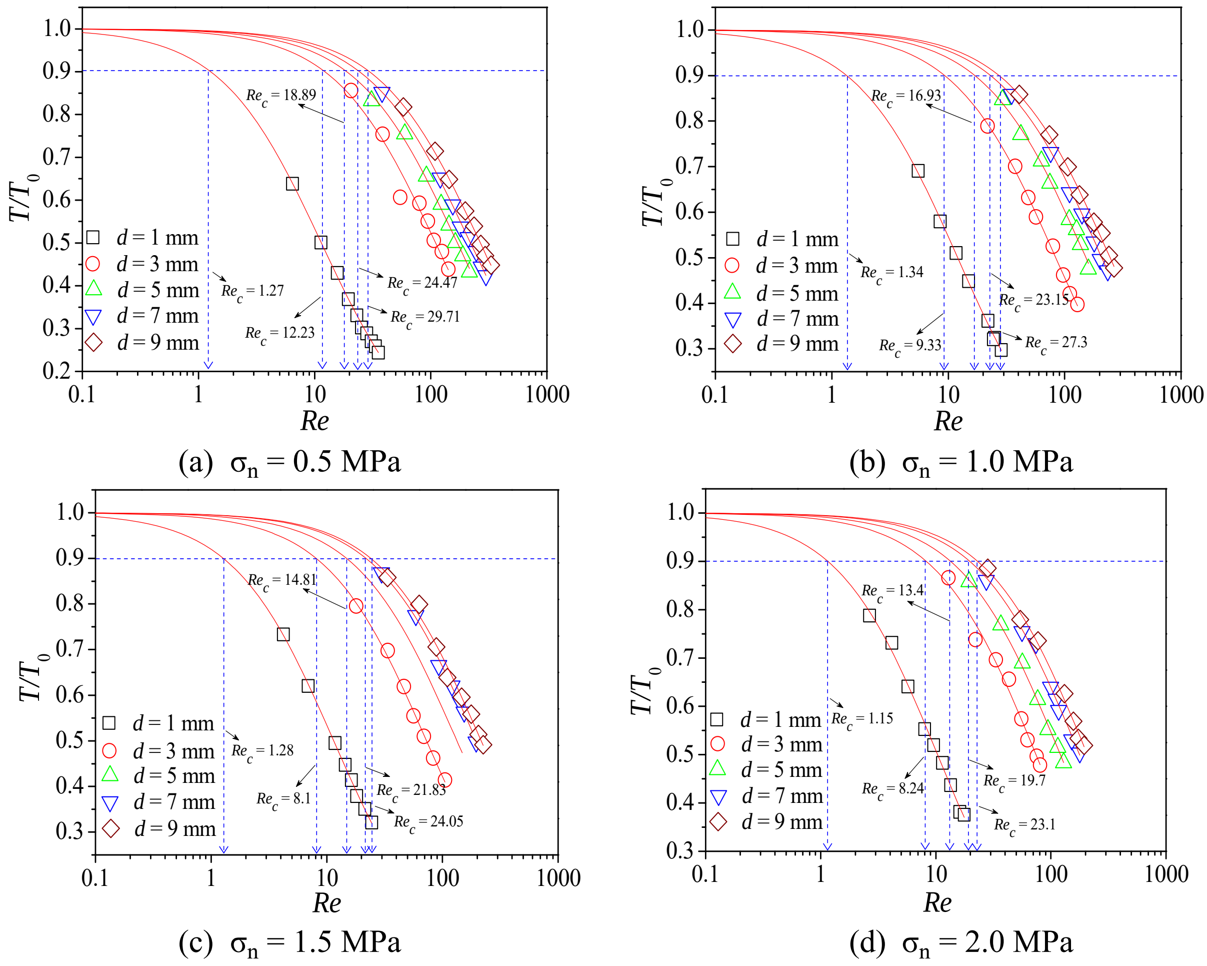

Fig. 14 Relationships between normalized transmissivity (T/T_0) and Reynolds number (Re) for G4 under different normal stresses.

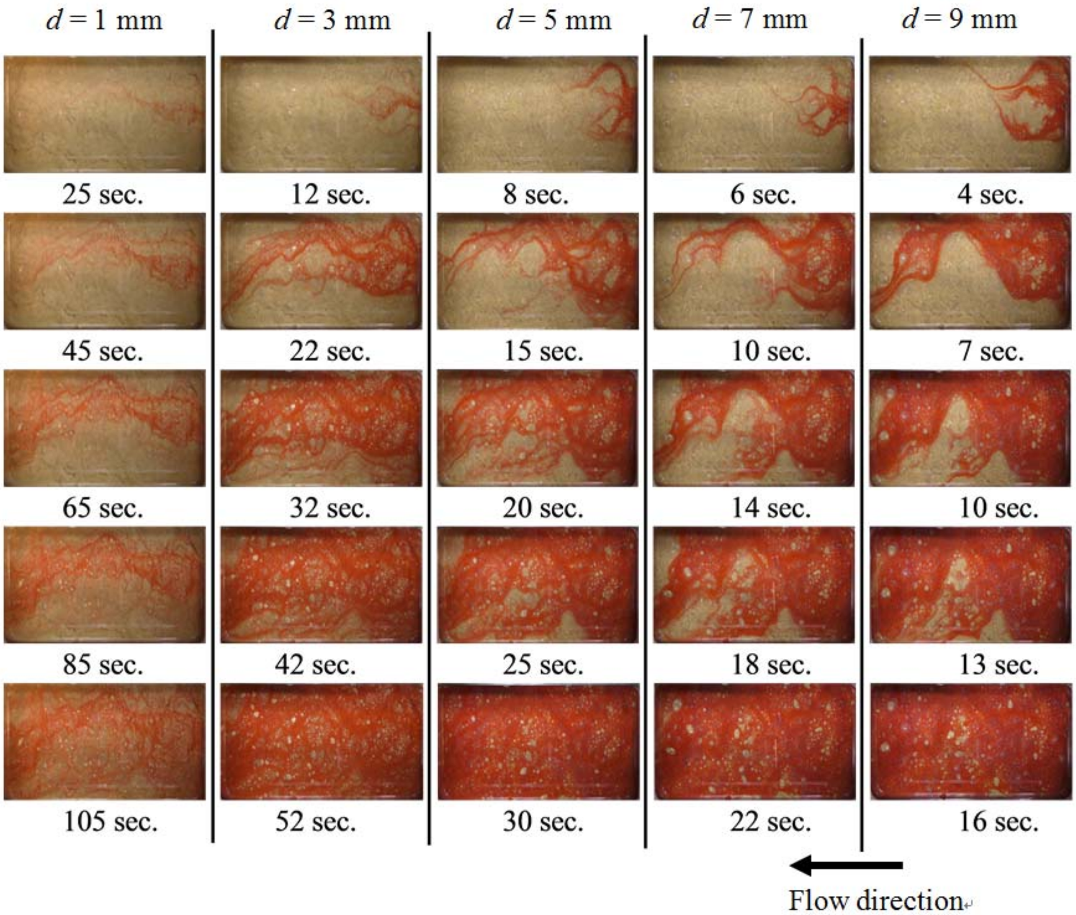

Fig. 15 Visualizations of the process of fluid flow in specimen G3-1 at different shear displacement.

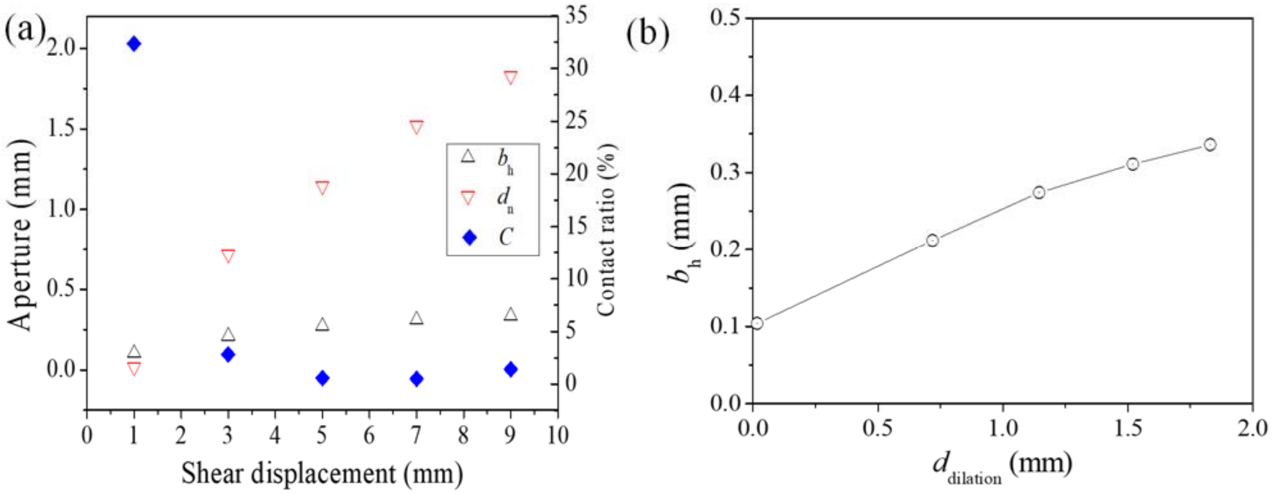

Fig. 16 (a) Evolution of hydraulic aperture b_h, dilation $d_{dilation}$ and contact ratio C of the specimen G3-1 during shear. (b) Relationship between hydraulic aperture b_h and dilation $d_{dilation}$.

Appendix A

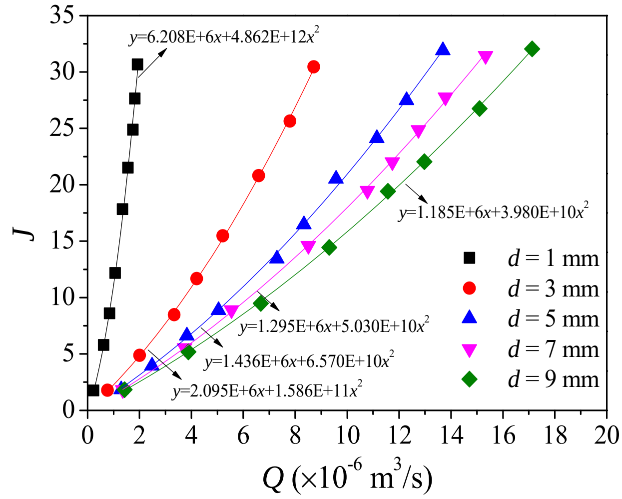

(a) G2 σ_n = 0.5 MPa

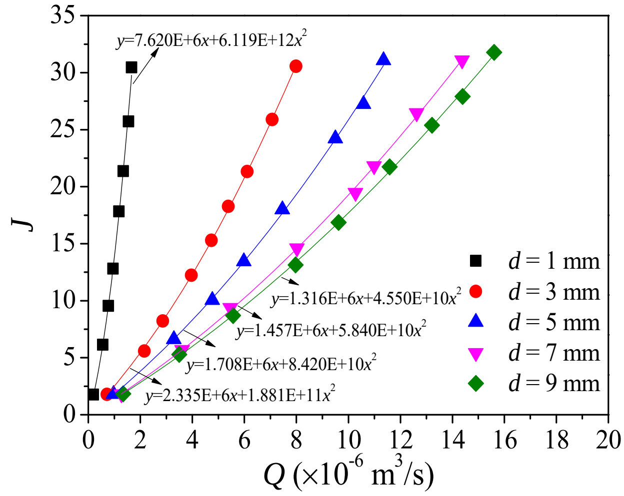

(b) G2 σ_n = 1.0 MPa

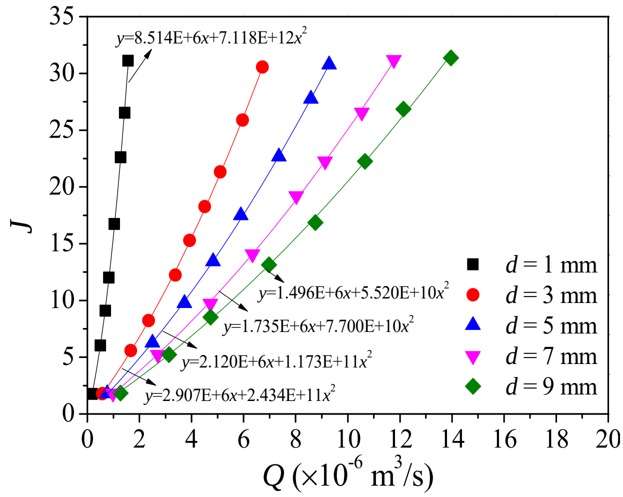

(c) G2 σ_n = 1.5 MPa

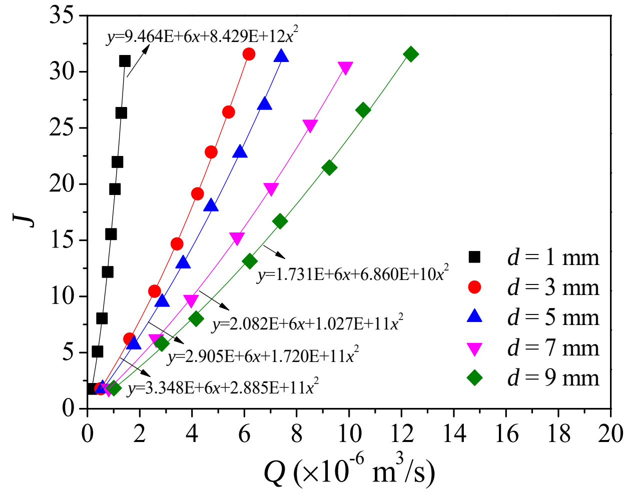

(d) G2 σ_n = 2.0 MPa

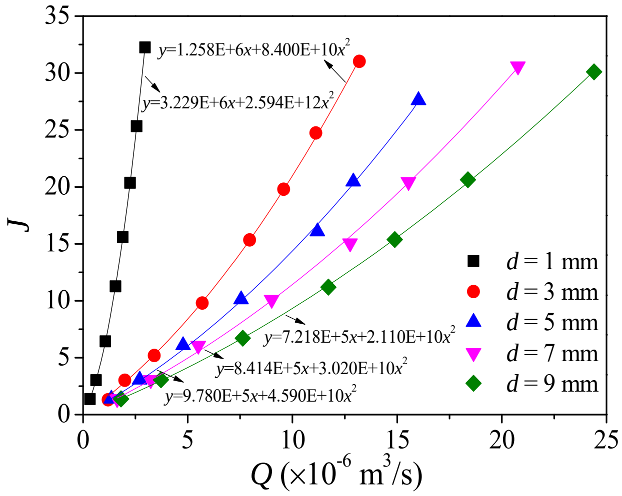

(e) G3 σ_n = 0.5 MPa

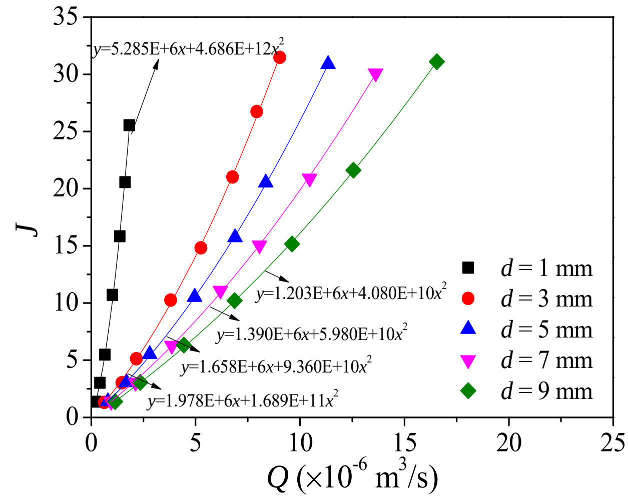

(f) G3 σ_n = 1.0 MPa

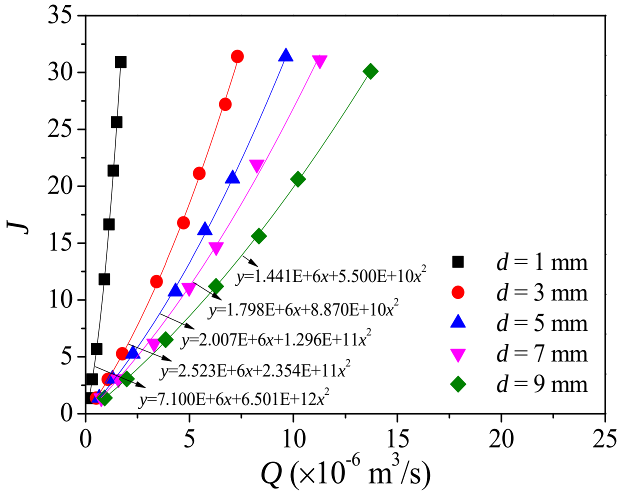

(g) G3 σ_n = 1.5 MPa

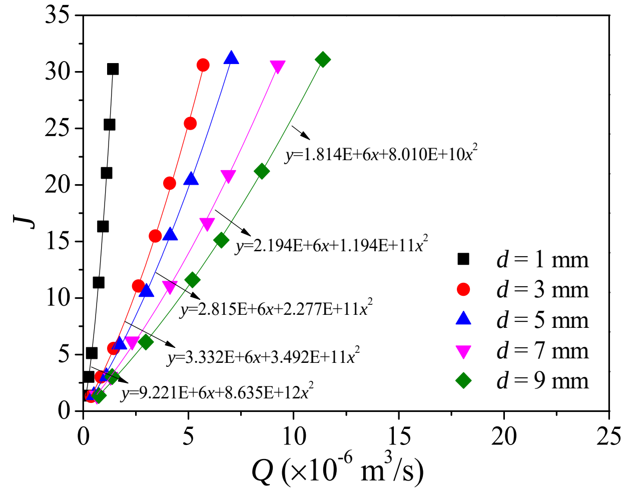

(h) G3 σ_n = 2.0 MPa

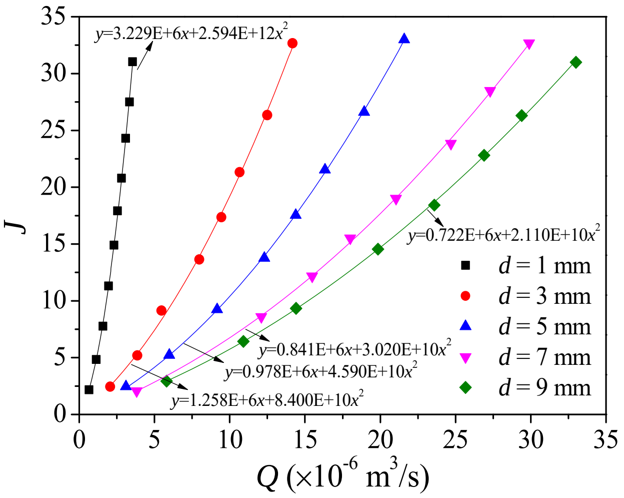

(i) G4 σ_n = 0.5 MPa

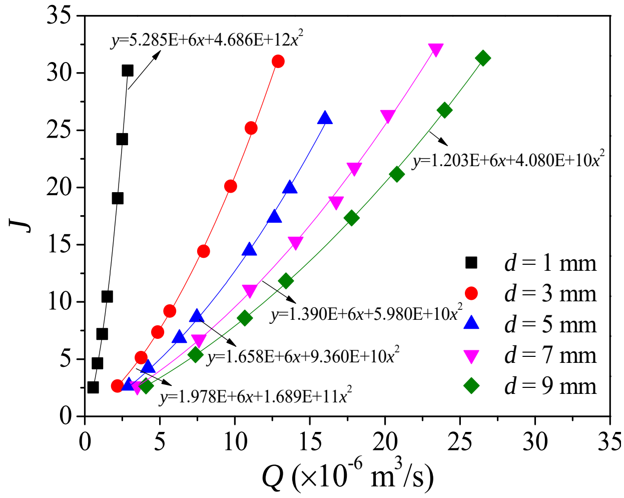

(g) G4 σ_n = 1.0 MPa

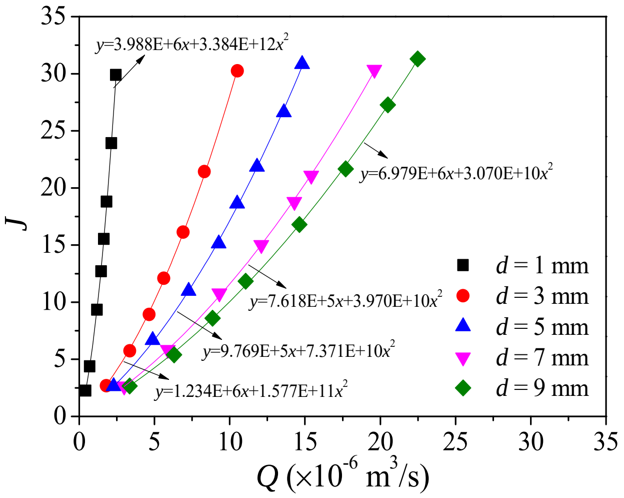

(k) G4 σ_n = 1.5 MPa

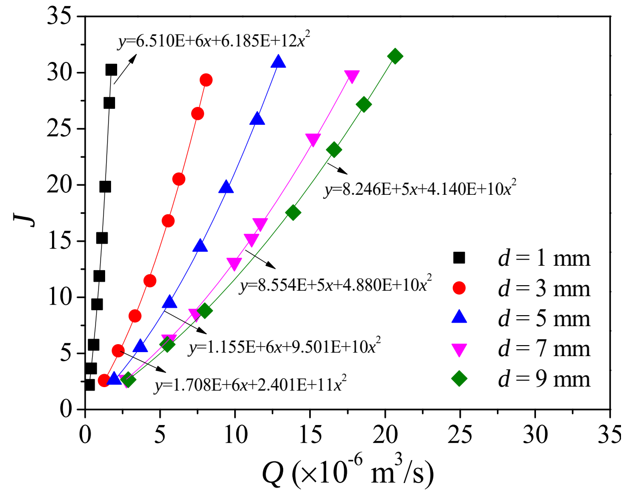

(l) G4 σ_n = 2.0 MPa

Fig. A1. Relationships between hydraulic gradient (J) and volumetric flow rate (Q) for G2-G4 under different normal stresses.